JGP Journal of General Physiology

ARTICLE

A novel theoretical framework reveals more than one voltage-sensing pathway in the lateral membrane of outer hair cells

Brenda Farrell, Benjamin L. Skidmore, Vivek Rajasekharan, and William E. Brownell

Outer hair cell (OHC) electromotility amplifies acoustic vibrations throughout the frequency range of hearing. Electromotility requires that the lateral membrane protein prestin undergo a conformational change upon changes in the membrane potential to produce an associated displacement charge. The magnitude of the charge displaced and the mid-reaction potential (when one half of the charge is displaced) reflects whether the cells will produce sufficient gain at the resting membrane potential to boost sound in vivo. Voltage clamp measurements performed under near-identical conditions ex vivo show the charge density and mid-reaction potential are not always the same, confounding interpretation of the results. We compare the displacement charge measurements in OHCs from rodents with a theory shown to exhibit good agreement with in silico simulations of voltage-sensing reactions in membranes. This model equates the charge density to the potential difference between two pseudo-equilibrium states of the sensors when they are in a stable conformation and not contributing to the displacement current. The model predicts this potential difference to be one half of its value midway into the reaction, when one equilibrium conformation transforms to the other pseudo-state. In agreement with the model, we find the measured mid-reaction potential to increase as the charge density decreases to exhibit a negative slope of ~1/2. This relationship suggests that the prestin sensors exhibit more than one stable hyperpolarized state and that voltage sensing occurs by more than one pathway. We determine the electric parameters for prestin sensors and use the analytical expressions of the theory to estimate the energy barriers for the two voltage-dependent pathways. This analysis explains the experimental results, supports the theoretical approach, and suggests that voltage sensing occurs by more than one pathway to enable amplification throughout the frequency range of hearing.

Introduction

Sound deflects the cochlear partition to produce a traveling wave along the basilar membrane. The motion of the basilar membrane is amplified by an axial force that merges with the basilar membrane velocity to deliver power to the fluid-filled cochlea (Dong and Olson, 2013). Force (Iwasa and Adachi, 1997) is produced by outer hair cells (OHCs; Brownell et al., 1985) that form part of the specialized epithelia of the organ of Corti. The origin of the force is in part due to the specialized properties of the lateral wall (Forge, 1991; Holley and Ashmore, 1990; Holley et al., 1992; Legendre et al., 2008; Tolomeo et al., 1996; Triffo et al., 2019) and the membrane protein prestin (Zheng et al., 2000), found abundantly (Mahendrasingam et al., 2010) within the lateral wall membrane. The voltage sensor prestin, i.e., SLC26A5, belongs within the superfamily of solute carriers (SLCs) and subfamily of anion exchangers, SLC26. This membrane protein is sensitive to changes in membrane tension (Adachi and Iwasa, 1999; Kakehata and Santos-Sacchi, 1995) and membrane voltage, with the latter most commonly investigated experimentally at constant membrane tension. The protein (together with other components of the voltage sensor) undergoes a conformational change upon changes in the membrane potential. One consequence of this conformational change is the production of a force and associated displacement charge (Santos-Sacchi, 1991), which is enormous (Santos-Sacchi et al., 1998) because of the attomoles of prestin sensors present in the lateral membrane of each OHC.

The molecular entity responsible for the displacement charge is not resolved. Structure–function studies of the membrane protein prestin suggest the transmembrane domain exhibits a 7 + 7 inverted structural repeat (Gorbunov et al., 2014). This

Bobby R. Alford Department of Otolaryngology and Head & Neck Surgery, Baylor College of Medicine, Houston, TX.

Correspondence to Brenda Farrell: bfarrell@bcm.edu.

© 2020 Farrell et al. This article is distributed under the terms of an Attribution–Noncommercial–Share Alike–No Mirror Sites license for the first six months after the publication date (see http://www.rupress.org/terms/). After six months it is available under a Creative Commons License (Attribution–Noncommercial–Share Alike 4.0 International license, as described at https://creativecommons.org/licenses/by-nc-sa/4.0/).

Check for updates

Downloaded from http://rupress.org/jgp/article-pdf/152/7/e201912447/1801126/jgp_201912447.pdf by guest on 09 February 2026

tertiary structure prediction was later supported by the crystal structure of a bacterial SLC26 homologue, SLC26Dg (Geertsma et al., 2015), that is found in the same subfamily of anion exchangers as prestin. Each half of this inverted repeat structure contributes to a core and gate subdomain with the core suggested to harbor both a charge center and an anion-binding site (Gorbunov et al., 2014). Other reports suggest that different charge regions (Kuwabara et al., 2018; Tan et al., 2012), i.e., not the core, may contribute to the displacement charge. Indeed, whether charged amino acids of prestin (Bai et al., 2009; Rybalchenko and Santos-Sacchi, 2008), intracellular anions (Oliver et al., 2001), or both anions and amino acids (Muallem and Ashmore, 2006) are the physiological voltage sensor is controversial. Likewise, the quaternary structure of the protein is not established. Some suggest it is a dimer (Bian et al., 2010; Detro-Dassen et al., 2008; Zheng et al., 2006), while others suggest that the protein within the plasma membrane is more likely to be a tetramer (Hallworth and Nichols, 2012; Wang et al., 2010). Our stoichiometric analysis and those of others (Homma and Dallos, 2011) suggest that each monomer (of the putative multimer) contributes to the displacement charge.

We do know from a multitude of electrophysiology experiments that the product of the charge movement (ne_o) along the reaction coordinate (δ), i.e., normal to the membrane (see Eq. 5), ranges from 0.72 to 0.99 elementary charges (e_o). We also know that the total amount of displacement charge per OHC for rodents is between 5 and 40 attomoles of charge and depends on the linear capacitance of the lateral membrane, albeit not always linearly (Corbitt et al., 2012; Mahendrasingam et al., 2010; Santos-Sacchi et al., 1998). The voltage when half of the charge has moved, $V_{0.5}$ (i.e., peak potential or mid-reaction potential or setpoint), appears to be the most capricious parameter. It depends on the membrane tension (Kakehata and Santos-Sacchi, 1995), the lipid composition of the membrane (Rajagopalan et al., 2007; Sfondouris et al., 2008), phosphorylation (Deák et al., 2005; Frolenkov et al., 2001), and glycosylation (Matsuda et al., 2004; Rajagopalan et al., 2010), and was found to increase from base to apex across the cochlea for one mouse colony (Zhu et al., 2013). Understanding the variable nature of this voltage is relevant biologically, as this potential is expected to be close to the resting (or silent) potential of the cell (Cody and Russell, 1987; Dallos, 1985; Johnson et al., 2011; Russell and Kössl, 1992). Likewise, the charge density, $\frac{Q_T^m}{C_{LW}}$, where Q_T^m is maximum measured charge per cell and C_{LW} is the measured lateral membrane capacitance per cell, is also commonly reported, and together with $V_{0.5}$ is an indicator of whether the animal will boost the sound in vivo (Patuzzi et al., 1989). We suggested that the charge density varies along the length of a cell (Corbitt et al., 2012), while others propose that charge density is highest in the middle and lower at the poles of the lateral membrane of an OHC (Santos-Sacchi, 2002). Mahendrasingam et al. (2010) found that the charge density and $V_{0.5}$ were independent of the positional origin (i.e., frequency) of the OHC within the cochlea of young albino rats.

Here, we show that $V_{0.5}$ is not capricious and that the observations can be explained within a theoretical framework (Kim and Warshel, 2015, 2016) that derives expressions from a Hamiltonian, which considers three components participating during a voltage clamp experiment: (1) the voltage-sensing protein; (2) the membrane; and (3) the surrounding electrolyte. This model determines the displacement charge by calculating the externally flowing charges in the surrounding electrolyte that arise from the charge movement occurring between two states of a voltage sensor in the membrane. The measured current in the circuit, $I_{circuit}$, is the current arising from the displacement charge from one sensor, I_D, and the linear current that results from charging the membrane,

$$I_{circuit} = I_D + C_{L,eq}\frac{dV}{dt}, \tag{1a}$$

where t is time, V is membrane potential, and $C_{L,eq}$ is the linear capacitance of the lipid bilayer where the protein sensor resides. That is, $C_{L,eq}$ represents the variance of the charge distributions of a voltage-sensing membrane protein, such as prestin when the sensor is in its quasi-equilibrium state, i.e., at a membrane potential when it is either very hyperpolarized (deactivated) or very depolarized (activated) and not contributing to I_D. In the case of an OHC with N independent prestin sensors residing in the lateral membrane, Eq. 1a is written as

$$NI_{circuit} = NI_D + C_{LW}\frac{dV}{dt}, \tag{1b}$$

where $C_{LW} \equiv NC_{L,eq}$ and $C_{L,eq}$ is the linear membrane capacitance of the bilayer where one prestin voltage sensor resides. Note that C_{LW} or $C_{L,eq}$ are usually not the linear membrane capacitance measured in an electrophysiology experiment, but for the OHC, the magnitude of C_{LW} can be estimated from such experiments (Corbitt et al., 2012). This is important because a useful relationship was derived (Kim and Warshel, 2015, 2016) that connects the displacement charge (found by integration by time of the first term on righthand side of Eq. 1) to the product of $C_{L,eq}$ and the potential difference between the two quasi-equilibrium states. We use this fluctuation–dissipation-based relationship to explain the association between the charge density and the magnitude of the mid-reaction potential ($V_{0.5}$) for OHCs from rodents. This association reveals that there is more than one hyperpolarized state of the prestin sensor in the lateral membrane.

Also relevant biologically is the speed of the conformational change of prestin, especially given the recent proposition that OHCs' electromotility may not be the only process responsible for amplifying sound in vivo (Cooper et al., 2018; Vavakou et al., 2019). Conventional models predict that the conformational change should proceed at reaction rates ≥70–90 kHz (time constant ≤2 µs at 37°C) to not limit hearing, while considering that nonecholocating mammals exhibit a median limit of 52 kHz, with a maximum limit of 70–90 kHz for mice (Heffner et al., 2001). However, the only reported high-temporal-resolution measurement of charge displacement suggests that the rate is 16 kHz (time constant ~10 µs) at 26°C (Gale and Ashmore, 1997), although these data are sparse and the voltage dependence of the reaction was not explored. A more recent report also found a slower rate of 9–10 kHz (Santos-Sacchi and Tan, 2018), but the bandwidth of the instrument is unclear. These rates (Gale and

Downloaded from http://rupress.org/jgp/article-pdf/152/7/e201912447/1801126/jgp_201912447.pdf by guest on 09 February 2026

Ashmore, 1997; Santos-Sacchi and Tan, 2018) are three to five times lower than force production rates (50 kHz) produced by the cell (Frank et al., 1999). The speed of the conformational change will depend on the magnitude of the activation (hyperpolarized state to depolarized state) and deactivation (depolarized state to hyperpolarized state) barriers for the reaction ($\Delta G^{\S}$) determined at zero membrane potential $V \equiv 0$. For example, the well-studied K^+ channels exhibit relatively slow conformational changes (time constant ~5–30 ms, up to 32 Hz; Rodríguez et al., 1998) that are preceded by a faster event that reflects higher (24 $\kappa_B T$; Chowdhury and Chanda, 2012) and lower (8 $\kappa_B T$; Delemotte et al., 2015; Sigg et al., 2003) barriers (κ_B, Boltzmann's constant; T, temperature). The fastest indirect experimental estimate reported for a conformational change of any membrane protein is 860/ms (time constant of 1.16 µs, 137 kHz room temperature, $T \equiv 24°C$), which is the rate for conditions with no activation barrier, i.e., no uphill energy to overcome for the reaction to proceed (Chakrapani and Auerbach, 2005). The magnitude of the activation and deactivation energy barriers for the prestin-based voltage-sensing reaction are unknown. We will estimate the energy barriers for the first time by analyzing the electrophysiology data obtained from rodents with this theoretical framework (Kim and Warshel, 2015, 2016).

The paper is arranged as follows. We first summarize the theoretical model and the experimental methods. This is followed by a description of the charge displacement measured with OHCs isolated from two guinea pig colonies by electrophysiology techniques. This data and reported data (Cheatham et al., 2005; Homma et al., 2013; Mahendrasingam et al., 2010; Yamashita et al., 2012; Zhu et al., 2013, 2015) are then compared with the model, which provides evidence for two hyperpolarized states of the prestin sensor. The kinetic scheme and the energy barrier for each voltage-dependent pathway are then presented and physiological implications discussed. We end by presenting limitations of the data and the model.

Theoretical model

A voltage clamp experiment was simulated in silico for a protein (*Ciona intestinalis* voltage-sensitive phosphatase), where the 3D structure of the two states, i.e., activated and deactivated, and the molecular entity of the charge that moves are known. Simulation results (e.g., charge movement, mid-reaction potential, and barrier activation energy) were found to exhibit good agreement with closed-form analytical expressions (to second order; Kim and Warshel, 2016). We use their closed-form expressions to analyze OHC electrophysiology data after we express them in terms of the parameters obtained in such experiments.

The charge moved, q (in this case net positive displacement charge), is related to the product of the voltage-independent or linear capacitance of the bilayer where the protein sensor resides, $C_{L,eq}$ and the potential difference between two putative quasi-equilibrium states, ΔV_{min} :

$$q = C_{L,eq}\Delta V_{\min}, \tag{2a}$$

where $\Delta V_{\min} = V_d - V_h$, and V_d and V_h are the equilibrium (minimum) potentials when the voltage sensors are fully hyperpolarized, denoted by subscript h and fully depolarized denoted by subscript d (Eq. 33 of Kim and Warshel, 2016). After we rearrange Eq. 2a and write it in terms of this pseudo-equilibrium potential difference ΔV_{min} between the two states,

$$\Delta V_{\min} = \frac{q}{C_{L,eq}}, \tag{2b}$$

we note the righthand side of Eq. 2b is the charge density of one voltage sensor. We rewrite Eq. 2b in terms of experimentally measured parameters. Specifically, N independent prestin sensors that each exhibit a charge of q and with each residing on a membrane to exhibit a linear membrane capacitance of $C_{L,eq}$, that is

$$\Delta V_{\min}^{exp} = \frac{Nq}{NC_{L,eq}} \equiv \frac{Q_T^m}{C_{LW}}, \tag{2c}$$

where the superscript *exp* denotes the potential difference between the pseudo-states is determined experimentally. Note that $C_{L,eq}$ (and C_{LW}) is a linear capacitance, and equivalent to the quotient of the charge moved and the voltage difference between the two pseudo-minimum states of the sensor. Eq. 2 connects the quasi-equilibrium voltage for each state relative to the potential when each state is equally occupied, $V_{0.5}$. Then, for a sensor that transforms from one state to a second state via a symmetrical barrier (Eq. 58 in Kim and Warshel, 2016), an expression for the mean $V_{0.5}$ can be written in terms of the mean experimental charge density, Q_T^m/C_{LW}, (Eq. 2c) and the pseudo-potentials

$$V_{0.5} = V_d - \frac{1}{2}\Delta V_{\min}^{\exp} = V_d - \frac{1}{2}\frac{Q_T^m}{C_{LW}} \tag{3a}$$

and

$$V_{0.5} = V_h + \frac{1}{2}\Delta V_{\min}^{\exp} = V_h + \frac{1}{2}\frac{Q_T^m}{C_{LW}}. \tag{3b}$$

Combining Eq. 3a and Eq. 3b,

$$V_{0.5} \cong \frac{(V_h + V_d)}{2} \tag{3c}$$

Eq. 3 predicts that a plot of $V_{0.5}$ versus ΔV_{min}^{exp} would exhibit a constant mean Gaussian value for prestin voltage sensors that possess constant intrinsic properties, (i.e., $C_{L,eq}$, q, V_d, V_h, and $V_{0.5}$; case 1). If the prestin voltage sensors exhibit more than one hyperpolarized state, (e.g., V_h changes, but the depolarized state, V_d, is unchanged), then ΔV_{min}^{exp} would decrease as $V_{0.5}$ increases to exhibit a slope of –1/2 (case 2). Likewise, if the prestin voltage sensors exhibit more than one depolarized state, (e.g., V_d changes, but the hyperpolarized state, V_h, is unchanged), then ΔV_{min}^{exp} should increase as $V_{0.5}$ decreases to exhibit a positive slope of 1/2 (case 3). If the sensors are not identical and both pseudopotentials are not constant, then a plot of $V_{0.5}$ versus ΔV_{min}^{exp} will not exhibit a predictable relationship (case 4). We show that a plot of $V_{0.5}$ as a function of ΔV_{min}^{exp} has a negative slope, with an approximate value of one half for OHCs from rodents. This is evidence for more than one hyperpolarized state of the sensor.

The slope, δ in Eq. 3, represents the progress of the reaction at $V \equiv V_{0.5}$. For any membrane potential, the slope, δ in Eq. 3

Downloaded from http://rupress.org/jgp/article-pdf/152/7/e201912447/1801126/jgp_201912447.pdf by guest on 09 February 2026

describes the change, $\partial\Delta G^{\S}$, in the barrier energy, $\Delta G^{\S}$, for the reaction relative to the change $\partial\Delta G^{o}$ in standard Gibbs free energy, ΔG^{o}, for the reaction. An expression (Eq. 57 in Kim and Warshel, 2016) to calculate the slope, δ is

$$\delta = \frac{1}{2} + \frac{C_{L,eq}}{q}(V - V_{0.5}), \tag{4}$$

where at $V \equiv V_h$ then $\delta = 0$, $V \equiv V_d$ then $\delta = 1$, and $V \equiv V_{0.5}$ then $\delta = 0.5$. Note that δ is the fraction of the distance the charge has moved normal to the dielectric membrane and is related experimentally to the measured voltage sensitivity, α_B

$$\alpha_B \equiv \frac{1}{\kappa_B T} z e_o \equiv \frac{1}{\kappa_B T}(n\delta)e_o, \tag{5}$$

where e_o is elementary charge, n is the number of charges that move, and z is the product of n and δ ($z \equiv n\delta$), where we also note that δ is not estimated independently from n in electrophysiology experiments.

Eq. 2 was derived by calculating the voltage-dependent free energy of each state at each voltage in terms of the membrane capacitance (see Eq. 30 in Kim and Warshel, 2016), which facilitates the derivation of an expression for the solvent reorganization energy for charge transfer, λ. This represents the energy required to rearrange the environment (e.g., electrolyte), but without charge transfer actually occurring, and is

$$q^2 = 2C_{L,eq}\lambda, \tag{6a}$$

where the square of the charge increases with the product of the linear capacitance of the lipid bilayer wherein the protein sensor resides, and the solvent reorganization energy. In terms of the measured charge arising from millions of independent prestin sensors, we rewrite Eq. 6a upon multiplying each side by N^2 and rearranging

$$N^2q^2 = 2N^2C_{L,eq}\lambda,$$
$$(Q_T^m)^2 = 2N\lambda C_{Lw} = 2N\lambda C_{Lw}\frac{C_{L,eq}}{C_{L,eq}} = \frac{2\lambda}{C_{L,eq}}C_{LW}^2, \tag{6b}$$

where the square of the measured charge increases linearly with the square of the lateral wall capacitance.

We show here that we can estimate $C_{L,eq}$, $V_{0.5}$, and q for prestin sensors residing on the lateral membrane of OHCs from electrophysiological data and then estimate λ with Eq. 6a and the energy barrier ($\Delta G^{\S}$) with

$$\Delta G^{\S} = \frac{C_{L,eq}}{2}\left(V_{0.5} \mp \frac{q}{2C_{L,eq}}\right)^2, \tag{7}$$

where the negative and positive signs within the parentheses represent the activation (hyperpolarized to depolarized direction) and deactivation (depolarized to hyperpolarized) energy, respectively.

Expressions used to determine the experimental parameters needed to compare with the model

During an OHC electrophysiology experiment performed under constant experimental conditions (i.e., membrane tension, temperature, and ionic composition), we measured the four parameters needed to make use of expressions Eqs. 2, 3, 4, 5, 6, and 7, i.e., C_{LW}, Q_T^m, $V_{0.5}$, and α_B. The measured OHC membrane capacitance (C) is the sum of the linear (C_L) and voltage-dependent (C_{NL}) capacitance, where the linear capacitance encompasses both the capacitance of the lateral wall membrane (C_{LW}) where voltage-sensors reside and the capacitance of the nonlateral wall region (C_{NLW}),

$$C_L = C_{NLW} + C_{LW}. \tag{8a}$$

The nonlateral wall region includes the capacitance of the stereocilia bundle (C_{SB}), the basal pole (C_B), and the cuticular plate (C_{CP}; Corbitt et al., 2012; Fig. S1). C_L was calculated at voltages positive to the peak capacitance where the slope, $\partial C/\partial V$ (calculated for three to five consecutive data points) was close to zero, and C_{NL} was determined by subtracting C_L from the measured capacitance. We determined C_{NLW} by calculating the capacitance of the stereocilia bundle and plotting the maximum measured charge movement (Q_T^m) for each cell as a function of $[C_L\text{-}C_{SB}]$ to find the root $exp\left(-\frac{\gamma}{\beta}\right)$ of

$$Q_T^m = \beta\log[C_L - C_{SB}] + \gamma, \tag{8b}$$

where β and γ are constants determined experimentally. Then C_{NLW} is determined with

$$C_{NLW} = C_L - C_{SB} - (C_B + C_{CP}) \cong \left[C_L - C_{SB} - \exp\left(-\frac{\gamma}{\beta}\right)\right], \tag{8c}$$

and C_{LW} is then calculated with Eq. 8a (Corbitt et al., 2012).

The electrical parameters associated with the nonlinear capacitance (denoted by superscript m) were determined directly from the data. Q_T^m was determined by integrating the C_{NL} over the membrane voltage range $-0.18 < V < 0.18$, i.e., $Q_T^m = \sum_{i=1}^{N_p} C_{NL}^i(V^i)dV \equiv \sum_{i=2}^{N_p} Q_{NL}^i(V^i)$, where dV approximately equals 0.003 V, C_{NL}^i and Q_{NL}^i are the voltage-dependent capacitance, and charge measured at potential V^i, and N_P is the total number of points (100–200). The $V_{0.5}$ and the peak capacitance, $C_{peak,}^m$ were determined from a plot of C as a function of membrane potential, V (Fig. S1). The maximum voltage sensitivity, $\alpha(V_{0.5})$, was determined from the derivative of the normalized measured charge $\left(\frac{Q_{NL}^i}{Q_T^m}\right)$, i.e., $\left\{\alpha(V_{0.5}) = max\left[\partial\left(\frac{Q_{NL}^i}{Q_T^m}\right)/\partial V\right]\right\}$, where the voltage sensitivity α_B was then determined with

$$\alpha_B = \left\{\max\left[\partial\left(\frac{Q_{NL}^i}{Q_T^m}\right)\Big/\partial V\right]\right\} \times 4. \tag{8d}$$

Materials and methods

Electrophysiological data were curated as described (Farrell and Bengtson, 2019) and are available from Collaborative Research in Computational Neuroscience repository http://crcns.org/data-sets/ear/ear-1.

Animals and OHC isolation

Animals from two colonies were used in this study. The animals from the first colony were multicolored (pigmented) guinea pigs bred at Baylor College of Medicine and supplemented with animals purchased from Elm Hill Laboratories. The animals from the second colony were albino guinea pigs purchased from Charles River. Baylor College of Medicine Animal Care and Use Committee approved the care and use of animals.

Downloaded from http://rupress.org/jgp/article-pdf/152/7/e201912447/1801126/jgp_201912447.pdf by guest on 09 February 2026

Guinea pigs were classified based on sex and sexual maturity. Animals were considered prepubertal (juvenile) if either their age was less than postnatal day 35 (p35) or weight was <426 g (males) or <361 g (females). Electrophysiological data were obtained from 9 albino (475–632 g) and 15 pigmented (405–960 g) adult males; 14 albino (306–400 g) and 5 pigmented (240–390 g) prepubertal males; 9 albino (249–356 g) and 11 (210–340 g) pigmented prepubertal females, and 1 pigmented adult female (800 g). For the females, sexual maturity was also monitored by ensuring the vaginal closure membrane had not yet opened (Joshi et al., 1973; Stockard and Papanicolaou, 1919). We also used the periodic opening of the vaginal closure membrane to monitor the estrous stage of the adult females. The adult female was sacrificed at midphase.

Sequencing data were obtained from adult male pigmented (three animals; 40–70 d; 500–700 g; five cochleae); prepubertal female pigmented (five animals; 16–28 d; 250–400 g; eight cochleae); and prepubertal female albino (four animals; 23–30 d; 210–260 g, eight cochleae) guinea pigs.

Electrophysiological data were obtained from 89 OHCs, namely 39 (17 albino and 22 pigmented) from adult males, 21 (15 albino and 6 pigmented) from prepubertal males, 28 (10 albino and 18 pigmented) from prepubertal females, and 1 pigmented from an adult female. All electrophysiological data were collected within 47 to 182 min after sacrificing the animals, with a mean time of recording after sacrifice of 125 ± 32 min (pigmented) and 112 ± 36 min (albino; Table S1). OHCs were isolated and separated by cochlear turns (Corbitt et al., 2012), except for one cell whose turn was not identified.

Sequencing the prestin gene from cochleae of *C. porcellus*

Sequencing was conducted on cochlear tissue extracted from guinea pigs. Temporal bones were removed and the bullae were immersed and then dissected in RNAlater (Thermo Fisher Scientific). Each bulla was opened to visualize the cochlea, the otic capsule was removed, and the modiolus was cut at the base below the first turn. The extracted cochlea was then stored in RNAlater at −20°C. To isolate RNA, frozen cochleae (2–5 cochleae) were suspended in liquid nitrogen and homogenized with a pestle. RNA was extracted with RNeasy Lipid Tissue Mini Kit (Qiagen) and RNase-Free DNase Set (Qiagen) per instructions and assayed by monitoring the UV absorbance relative to control (no tissue added) with a Cytation 3 imaging reader (BioTek Instruments).

Single-strand cDNA was synthesized for quantitative RT-PCR from ∼1 µg of RNA with SuperScript III First-Strand Synthesis SuperMix (Invitrogen, Thermo Fisher Scientific) per instructions and purified with DNA Clean and Concentrator (Zymo Research Corp.). Primers were chosen based on prestin FASTA sequence of isoform *X1* of *C. porcellus* (Table S2), with 100 bp upstream and 50 bp downstream included in the BLAST (Basic Local Alignment Search Tool) search. One primer set was chosen to flank exon 4, which is missing in isoform *X3* (primer set 1), and two additional sets were chosen that flank exon 12 (primer sets 3A and 3B), which is missing in isoform *X2*. Each PCR reaction contained the same concentration of reactants at a total volume of 25 or 50 µl. The reactants (for 25 µl) were 40 ng of single-strand cDNA, 10× PCR mix (2.5 µl), 10 mM dNTPs (0.75 µl), 10 µM primers (forward and reverse each 0.75 µl), and Pfx50 DNA polymerase (0.5 µl), made up to final volume with sterile water. The time and temperature, *T*, of the reaction steps were initial denaturation (94°C for 5 min); 35 cycles of denaturation (94°C for 15 s/cycle), annealing (*T* dependent on the primer set for 30 s, Table S1), extension (68°C for 1 min), final extension (68°C for 5 min), and conservation (4°C). The molecular weight of products was determined by electrophoresis on 1.5% agarose gel, where all bands detected were processed and then sequenced with Applied Biosystems 3130XL Genetic Analyzer at the DNA sequencing and Gene Vector Core at Baylor College of Medicine.

Whole-cell patch-clamp voltage clamp assay

Chemicals were purchased from Sigma-Aldrich, except XE991, which was obtained from Tocris Bioscience. Dissection solution contained (in mM): 147 NaCl, 5.5 KCl, 10 HEPES, 2 $CaCl_2$, and 2.5 $MgCl_2$. Extracellular solution contained (in mM): 20 CsCl, 105 NaCl, 10 HEPES, 2 $CoCl_2$, 1.5 $MgCl_2$, 2 $CaCl_2$, and 20 $(CH_3\text{-}CH_2)_4NH_4Cl$. The solution in the patch-pipette contained (in mM): 140 CsCl, 2 $MgCl_2$, 10 EGTA, and 10 HEPES. In three experiments, the intracellular chloride concentration was 10 mM, with glutamate as the dominant anion in solution. Cesium glutamate was prepared by titrating glutamic acid (Sigma 232068; 1 M) with CsOH (1 M) until the pH of the solution reached 7.0. The composition of this solution within the patch pipette was (in mM): 133 $CsC_5H_8NO_4$, 6 CsCl, 2 $MgCl_2$, 10 EGTA, 10 HEPES, and 1 Cs_2CO_3. All solutions were adjusted to pH 7.2 with CsOH or NaOH, and osmolality was adjusted to 300 ± 2 mOsm kg^{-1} with D-glucose. The extracellular solution containing XE991 was perfused into the bath to a final concentration of 30–60 µM at least 5 min before recording. The pipettes were made of fused quartz, formed by use of a laser-based puller (Sutter Instruments), coated with Sylgard (Dow Corning), and exhibited resistances between 2 and 6 MΩ.

The size of each cell was measured from a bright-field image of the OHC obtained before the electrophysiological measurement (Corbitt et al., 2012). All experiments were conducted at room temperature and at a constant pipette pressure of 0 ± 0.1 kPa, which was maintained by use of a high-speed pressure clamp (HSPC-1; ALA Scientific Instruments). The membrane capacitance was calculated from the measured electrical admittance with a two-sine stimulus (Corbitt et al., 2012; Farrell et al., 2006), where we usually report the membrane capacitance calculated at the lower of the two frequencies. Values of membrane (R_m) and series (R_s) resistances were determined from the electrical admittance at positive voltages (typically 0.09–0.15 V) where there was no measurable voltage-dependent capacitance. Most recordings (81 of 89 cells) exhibited an $R_s < 10$ MΩ; the rest (8 of 89 cells) exhibited an $R_s < 12$ MΩ. The DC conductance was measured between −0.1 and 0.1 V with a voltage step-function (Farrell et al., 2006). $V_{0.5}$ was corrected for the voltage drop across the pipette by calculating the product of $V_{0.5}$ and $R_m/(R_s + R_m)$. The ratio was calculated either with DC conductance measured at the same voltage as the $V_{0.5}$ or with the conductance measured from the admittance at a voltage when there was no detectable voltage-dependent capacitance.

Downloaded from http://rupress.org/jgp/article-pdf/152/7/e201912447/1801126/jgp_201912447.pdf by guest on 09 February 2026

Algorithms written in LabVIEW (version 8.5.1; National Instruments) controlled the stimuli and data acquisition. Data analysis and statistics were performed with Matlab v8.2–v9.0 (Mathworks) and JMP (v 7.02, SAS Institute).

Molecular modeling and pKa prediction

The I-TASSER protein structure and function prediction server was used to produce a model of prestin that would permit size estimation and pKa analysis (Roy et al., 2010; Yang et al., 2015; Zhang, 2008). This predictive method uses sequence homology–based templates to construct full-length models from fragments of these templates. The bacterial fumarate transporter SLC26Dg (Protein Data Bank [PDB] accession no. 5DA0; Geertsma et al., 2015) was used as a template for the transmembrane and STAS domains, because it is homologous with prestin, SLC26A5. The coordinates for rat STAS domain (PDB accession no. 3LLO) are known (Pasqualetto et al., 2010) and were used as constraints in this predictive model. Because prestin has areas with no acceptable sequence alignment (38% of sequence length), I-TASSER implements ab initio modeling (Yang et al., 2015) for these regions. The templates and the template-free modeled regions were used to construct spatial restraints and guide model refinements. These simulations generated five clusters from which one structure from each cluster was selected based on the highest confidence score (C-score; Yang et al., 2015). This highest C-score correlates to RMSD. The model with the highest C-score was selected for size analysis and pKa prediction. Structural models were made from the sequence of human, guinea pig, rat, and gerbil prestin, and the transmembrane domain of guinea pig. A 3D molecular surface was generated around the transmembrane domain of each model based on the van der Waals size of each atom. To determine the dimensions of the transmembrane domain, the scale-bar overlay tool in Chimera was used to measure the distance between the two farthest points.

Titratable residues of this model were surveyed for pKa shifts with PROPKA 3.0 running on the PDB2PQR server (Dolinsky et al., 2004; Olsson et al., 2011). Residues that were not completely buried (i.e., solvent-accessible with two cutoffs at 90 and 25%) were used to estimate the net charge within the domains of our predicted model, assuming pH 7.2. The fit of the model into the membrane was achieved with the Orientation of Proteins in Membranes (OPM) server (Lomize et al., 2012). The model was visualized with Chimera (v.1.11; Pettersen et al., 2004).

Online supplemental material

Table S1 provides the mean times of electrophysiology recordings of OHCs relative to the lifetime temporal boundary of the animal. Table S2 lists primers used to sequence the prestin gene from *C. porcellus*. Table S3 shows the average charge density by cochlear region. Table S4 shows the predicted charge of topology models of prestin. Fig. S1 contains electrophysiology data obtained from one OHC showing the definition of measured parameters and magnitude of the calculated two pseudo-potentials. Fig. S2 shows measured voltage sensitivity for OHCs from two guinea pig colonies. Fig. S3 shows results upon sequencing the prestin gene and separating the PCR products by electrophoresis. Fig. S4 shows mid-reaction potential as a function of charge density where experimental data are grouped in smaller bins. Fig. S5 shows the specific capacitance of membrane determined at negative voltages. Fig. S6 is a model of the transmembrane region of guinea pig prestin within a bilayer and predicted with the OPM server. Fig. S7 is a comparison of hearing loss with experimental charge density in mice from wild type and engineered animals.

Results

Experimental magnitude of C_{LW}, Q_T^m, α_B, and $V_{0.5}$ in OHCs of two guinea pig colonies

The capacitance of the nonlateral wall region was found to be ~4.82 pF and is similar to that previously reported (4.86 pF) when only cells isolated from adult male guinea pigs were considered (Corbitt et al., 2012). We found no differences when cells were isolated from animals of either phenotype or when cells were isolated from adult or juvenile animals with this dataset. The capacitance of the lateral membrane ranged from 5.0 (± 2.4) pF for cells that originate from turn 1 to 17.9 (± 2.74) pF for cells from turn 4. Had the sensors on the lateral membrane been identical and independent, then Eq. 6b predicts that Q_T^M should increase linearly with C_{LW}. In contrast, Q_T^M increases with the logarithm of lateral wall capacitance (Corbitt et al., 2012), or the square of the charge increases much more steeply with C_{LW}^2 for sensors found on basal originating cells (C_{LW} < 10 pF) than for sensors found on the apical originating cells (Fig. 1). We proposed that the change in the slope, $\frac{\partial Q_T^M}{\partial C_{LW}}$ implies that the charge density varies along the length of the cell (Corbitt et al., 2012) and now suggest that this variation in charge density arises because λ and $C_{L,eq}$ are not constant for the prestin sensors on each OHC.

We found the maximum voltage sensitivity $\alpha(V_{0.5})$ for OHCs originating from pigmented animals (8.62 ± 0.95 V^{-1}) to be significantly greater (P < 0.0001; number of observations, 28) than $\alpha(V_{0.5})$ observed for cells isolated from albinos (7.65 ± 0.88 V^{-1}; number of observations, 41). In addition, we found that the maximum voltage sensitivity decreases across the cochlea from the base (9.32 ± 0.69 V^{-1}) to apex (8.08 ± 0.76 V^{-1}) for OHCs isolated from pigmented animals, with no gradient (basal, 7.76 ± 0.98 V^{-1}; apical, 7.59 ± 0.83 V^{-1}) observable for OHCs isolated from albinos (Fig. S2). This latter observation of cells from albinos is in agreement with earlier reported measurements (Santos-Sacchi et al., 1998). The positional differences between basal and apical regions for cells from pigmented animals are statistically significant. We determined α_B with corresponding $z \equiv n\delta$ calculated with Eq. 5 for experiments performed at 24°C (Table 1). When α_B is plotted as a function of lateral membrane capacitance, it decreases monotonically for cells from pigmented animals, with no relationship observed for the population of cells isolated from albinos (Fig. S2). The observations were similar when experiments were conducted with an additional potassium channel blocker (XE991) in the bath, which is selective for the KCNQ family (Table 1). Therefore, we grouped the results (XE991 and no XE991) from cells obtained from pigmented animals and calculated the mean α_B and z for cells

Downloaded from http://rupress.org/jgp/article-pdf/152/7/e201912447/1801126/jgp_201912447.pdf by guest on 09 February 2026

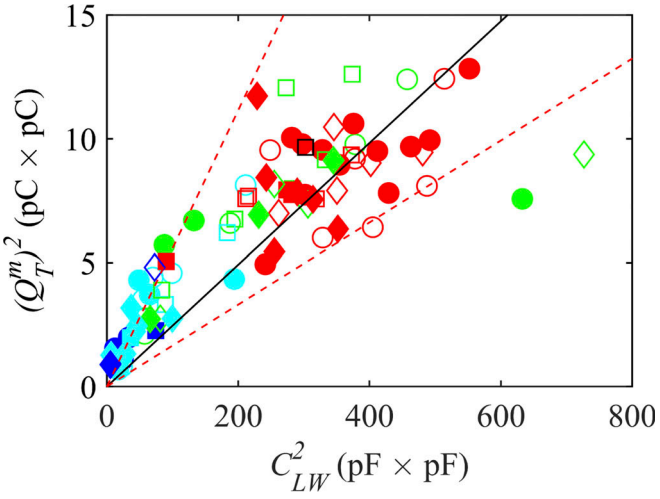

Figure 1. **Comparison of Eq. 6b (solid black line, adjusted R^2 of 0.516) to data assuming identical and independent voltage sensors in the membrane.** Closed and open symbols represent OHCs from normal mammalian phenotype (pigmented) and albino guinea pigs. Open circles, diamonds, and squares represent OHCs from adult males, juvenile males, and juvenile females, respectively. Colored symbols (blue, cyan, green, and red) represent OHCs that originate from turns 1, 2, 3, and 4, and black symbols represent OHCs of unknown origin. 86 cells with 144 mM chloride in patch pipette are shown. The dashed red line (left) was calculated with Eq. 6b for λ of 3.95 $\kappa_B T$ and $C_{L,eq}$ 0.584 aF; the dashed red line (right) was calculated for λ of 2.16 $\kappa_B T$ and $C_{L,eq}$ 1.07 aF.

originating from basal and apical regions of 37.1 ± 2.5 V^{-1} (z, 0.95 ± 0.06; number, 16) and 32.9 ± 2.7 V^{-1} (z, 0.84 ± 0.07; number, 27). This observation of different sensitivity was not expected, nor has it been previously reported. Experiments conducted with OHCs extracted from mammals at room temperature have shown that α_B is constant across the cochlea (Mahendrasingam et al., 2010; Santos-Sacchi et al., 1998) at 28–32 V^{-1} for mice (Cheatham et al., 2005; Gao et al., 2007; Yamashita et al., 2012); 29–30 V^{-1} for guinea pigs (Corbitt et al., 2012; Santos-Sacchi et al., 1998); and 37 V^{-1} for gerbils (Wang et al., 2010), with the most sensitive reported value at 37–39 V^{-1} for OHCs from young rats (Mahendrasingam et al., 2010). Because splice variants are known to affect the voltage sensitivity of membrane proteins (Al-Sabi et al., 2013), we then investigated whether there was evidence for variants of prestin in the cochlea of our guinea pigs.

We performed PCR on the cDNA synthesized from RNA that was isolated from the cochlea of adult male and prepubertal female pigmented guinea pigs and compared it with that extracted from albinos. Primers were chosen to detect variants *X2* and *X3* of prestin (Table S2). Although there are no known splice variants with missing regions in the STAS domain of guinea pig, isoforms that have complete or partial deletions are reported for humans (Liu et al., 2003). Primer set 4 was designed to flank the STAS domain and to detect such putative deletions. The annealing temperature was selected such that it was 2–5°C lower than the melting temperatures of both primers. To confirm that no variants were present in these regions, we conducted additional experiments after lowering the annealing temperature by a further 1.3–2°C. In all experiments, only isoform *X1* was detected upon sequencing (Fig. S3). We conclude that splice variants cannot explain the voltage sensitivity gradient (Fig. S2 and Table 1).

Table 1. **Voltage sensitivity depends on the positional origin of OHCs from one guinea pig colony (normal mammalian phenotype)**

Cells and region	α_B (V^{-1})	z	OBS	P value
(a) basal	36.4 (1.5)	0.93 (0.04)	4	0.0227
(a) apical	33.8 (1.8)	0.86 (0.05)	11	
(b) basal	37.3 (2.7)	0.96 (0.07)	12	<0.0001
(b) apical	32.3 (3.0)	0.83 (0.08)	16	
(c) basal	31.3 (3.8)	0.80 (0.10)	11	0.5294
(c) apical	30.5 (3.4)	0.78 (0.09)	30	

P values determined with one-way ANOVA. (a) and (b) represent observations with cells extracted from animals of normal phenotype with and without XE991 in the bath, and (c) represents observations with cells extracted from albinos. ANOVA effect tests revealed no significant influence of adding XE991 to the bath (P value = 0.7551). The SD of the mean is shown in parenthesis. OBS, number of observations.

The normalized charge movement and the capacitance of the lateral membrane are plotted as a function of membrane potential in Fig. 2 a. $V_{0.5}$ is not constant but ranges from −0.083 ± 0.030 V for turn 1 to −0.050 ± 0.018 V for turn 4 cells extracted from albinos, and from −0.102 ± 0.019 V (turn 1) to −0.052 ± 0.020 V (turn 4) for cells extracted from a normal pigmented phenotype. When examining this parameter as a function of lateral membrane capacitance; $V_{0.5}$ increases monotonically with C_{LW}, becoming more positive as C_{LW} increases (Fig. 2 b). There is no statistical difference between the gradient observed for each phenotype. However, the linear relationship is better with cells from pigmented phenotype (adjusted R^2 of ∼0.6) compared with cells from albinos (adjusted R^2 of ∼0.2). A similar relationship was observed for OHCs extracted from mice, although reported in terms of the length of OHCs, where they found OHCs to exhibit a $V_{0.5}$ gradient of 1.6 µm/mV across the cochlea (Zhu et al., 2013). The gradient is more than that measured in cells from guinea pigs, at 0.7 µm/mV. This mismatch in the slopes between the two species disappears when examined on the frequency scale, rather than by length. Mice exhibit OHC lengths that range from 13 to 30 µm and function within a frequency range of 1 to 90 kHz (Keiler and Richter, 2001; Müller et al., 2005), whereas lengths for guinea pig OHCs range from 20 to 94 µm and function within a range of 0.06 to 43 kHz (Pujol et al., 1992; Wilson and Johnstone, 1975). This observation of a $V_{0.5}$ gradient is different from the study with OHCs from young albino rats where no gradient was observed across the cochlea; $V_{0.5}$ was similar for OHCs from apical and basal regions at −0.038 ± 0.03 V and −0.042 ± 0.03 V (Mahendrasingam et al., 2010).

OHCs exhibit significant membrane conductance even in the presence of channel blockers. Two problems can arise when voltage clamping with the whole-cell patch-clamp technique. A significant voltage drop across the patch pipette occurs (e.g., 26%

Downloaded from http://rupress.org/jgp/article-pdf/152/7/e201912447/1801126/jgp_201912447.pdf by guest on 09 February 2026

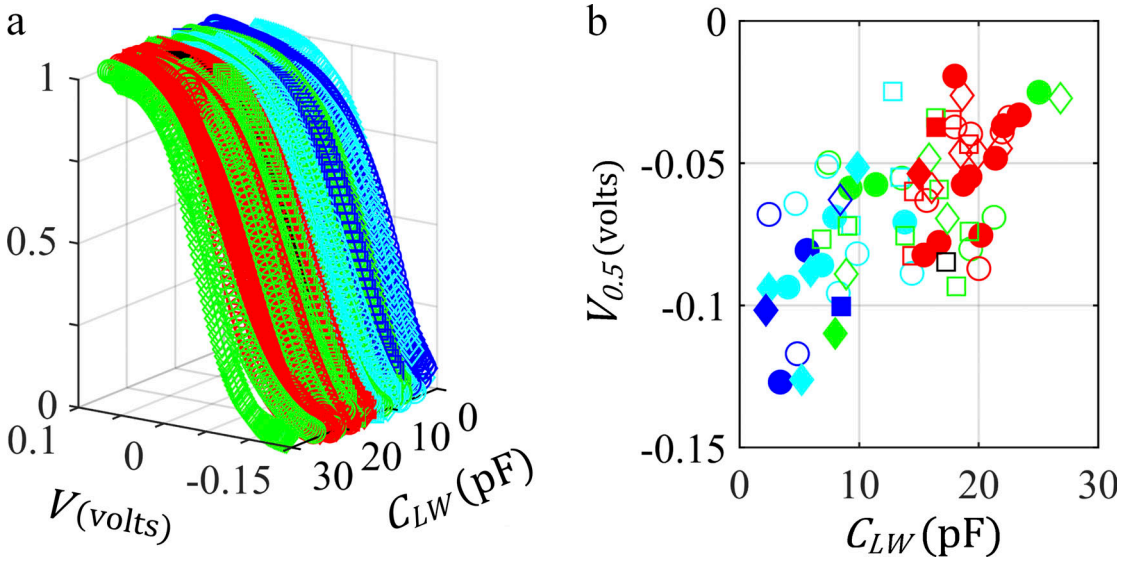

Figure 2. **$V_{0.5}$ depends on the positional origin of the cell for the guinea pig cochlea. (a)** Normalized charge for OHCs extracted from both phenotypes. **(b)** $V_{0.5}$ increases as lateral membrane capacitance increases. Cells with 144 mM chloride in patch pipette are shown (no XE991 added). Symbols are defined in Fig. 1. The number of cells plotted is 70.

at voltages >0.08 V) for OHCs and is a possible source of error on the voltage measurements, especially as the conductance varies with potential. Also, OHCs may not be space clamped along their length owing to their unique geometry. To check whether the trends and the scatter (Fig. 2) are related to these two problems, we conducted further measurements in the presence of XE991 at concentrations ≤60 µM, which is 10-fold its half-maximal inhibitory concentration (Yeung and Greenwood, 2005). When XE991 was added to the extracellular solution, it caused at least a twofold improvement in the voltage clamp, with the fractional drop consistently <13%. In addition, the conductance measured at $V_{0.5}$ in the presence of XE991 was as high as 335 pS, and the zero-current potential was more depolarized (V > 0.03 V, data not shown). We also report a surprising 20mV depolarizing shift of $V_{0.5}$ upon addition of XE991 (Table 2); this channel blocker did not affect the other electrical parameters. The increase in the magnitude of $V_{0.5}$ is not correlated with the voltage drop calculated at either $V_{0.5}$ or at positive voltages in the presence or absence of XE991, suggesting that the voltage drop across the pipette is a reasonable estimate and does not overtly affect the results.

Likewise, although there is theoretical (Rabbitt et al., 2009) and experimental (Nakagawa et al., 2006) evidence that OHCs may not be space clamped during whole-cell patch-clamp experiments, as they are long polarized cells and exhibit a nonuniform conductance (Ramamoorthy et al., 2013), a more recent report suggests that the OHC is isopotential (Song and Santos-Sacchi, 2015). This leads us to suggest at the concentrations used, XE991 causes a shift because of an interaction of XE991 with the voltage-sensory machinery to alter the chemical component of the energy. Independent of this observation, we provide evidence that Eq. 3a can describe the trends (Fig. 2) observed with and without XE991 in the bath.

Comparison of the experimental results with Eq. 3a

Shown in Fig. 3 is the mean charge density ΔV_{min}^{exp} plotted as a function of the mean $V_{0.5}$. The data were grouped (bin width 5 pF) based on the linear capacitance of the lateral membrane. We bundled the results for both mammalian phenotypes to improve the power, as the relationships were similar for both phenotypes. We then fitted the data to Eq. 3a, where V_d was the only free parameter, where the fit is shown as a blue dashed line in Fig. 3. When ΔV_{min}^{exp} < 0.25 V, the experimental data lies close to the central tendency of the theoretical line, but when ΔV_{min}^{exp} > 0.25 V, $V_{0.5}$ is larger than expected and exhibits greater variance (see Fig. S4 for data shown at higher resolution). Similar trends are found when ΔV_{min}^{exp} is calculated per cell and aggregated based on the positional polarity of the cell in the cochlea (Table S3). We

Table 2. **$V_{0.5}$ increases from base to apical region of cochlea and is sensitive to the addition of XE991**

Cells and region	$V_{0.5}$ (V)	OBS	P value
(a) basal	−0.062 (0.020)	4	0.0399
(a) apical	−0.035 (0.020)	11	
(b) basal	−0.091 (0.022)	12	0.0003
(b) apical	−0.054 (0.023)	16	
(c) basal	−0.071 (0.024)	11	0.0697
(c) apical	−0.057 (0.019)	30	

(a) and (b) represent measurements with cells extracted from normal phenotype with and without XE991 in the bath, and (c) represents measurements with cells extracted from albinos. The P value of the ANOVA is shown for each group. ANOVA effect tests on cells from a normal mammalian phenotype demonstrate the significant influence of adding XE991 to the bath (P value = 0.0035). The SD of the mean is shown in parentheses, OBS, number of observations.

Downloaded from http://rupress.org/jgp/article-pdf/152/7/e201912447/1801126/jgp_201912447.pdf by guest on 09 February 2026

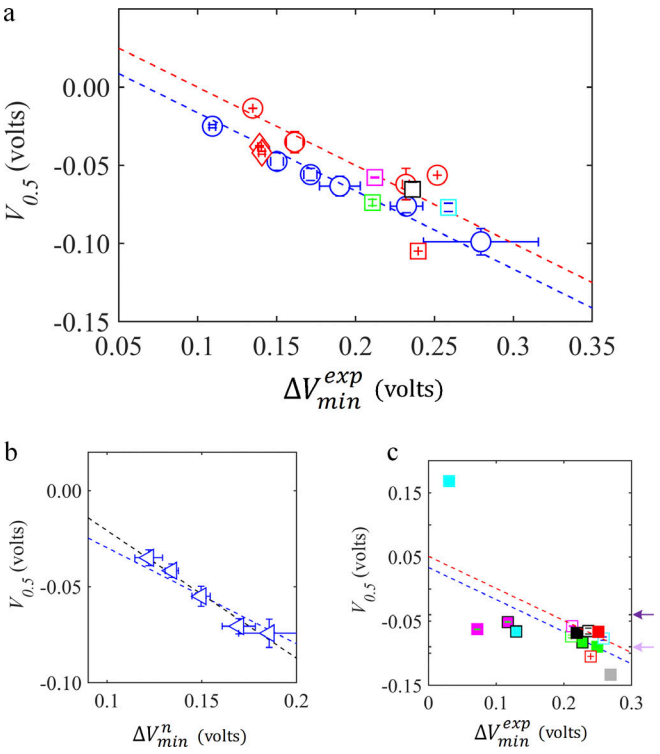

Figure 3. **Data from wild type rodents is described by Eq. 3a. (a)** $V_{0.5}$ increases as ΔV_{min}^{exp} decreases for measurements made without (open blue circles) and with (open red circles) 60 µM XE991 in the bath. The dashed blue line is the fit of data (open blue circles) to Eq. 3a with intercept, V_d 0.034 V (adjusted R^2, 0.916), and dashed red line is the fit of data (open red circles) to Eq. 3a with intercept, 0.0499 V (adjusted R^2, 0.793), where the number of data points was used as a weight in the fits. Bars represent SEM. Diamonds (red) represent data from albino rats (Mahendrasingam et al., 2010). Open squares represent data from mice in which C_{LW} was calculated from the surface area of the lateral membrane $2\pi r(l - r)$ from measurements of OHC length, l, and radius, r, with a specific membrane capacitance of 0.01 pF/µm. Black (Cheatham et al., 2005; r, 2.7 µm; l, 25 µm), cyan (Homma et al., 2013; r, 2.7 µm; l, 25 µm), magenta (Yamashita et al., 2012; r, 3.2 µm; l, 21.2 µm), green (Zhu et al., 2013; r, 3.5 µm; l, 19.04 µm), and red (Zhu et al., 2015; r, 3.0 µm; l, 17.5 µm). **(b)** $V_{0.5}$ as a function of ΔV_{min}^{n} determined at negative potentials (44 cells; no XE991 in the bath). The dashed blue line is the fit to Eq. 3a with an intercept at 0.02 V (adjusted R^2, 0.91). The dashed black line is the linear fit of data with a slope of −0.664 and an intercept at 0.046 V (adjusted R^2, 0.97). **(c)** Data from wild type animals are compared with data in which the mice were engineered to change key proteins. Cyan with black edge represents hzt/499, and cyan represents 499 KI (Homma et al., 2013); C_{LW} is the same as wild type. Magenta with black edge represents neo/neo (r, 3.15 µm; l, 19.06 µm), and magenta represents neo/prestin KO (r, 3.15 µm; l, 17.55 µm; Yamashita et al., 2012). Solid gray represents C1 KI (Gao et al., 2007); C_{LW} is the same as wild type reported in Homma et al. (2013). Solid green with black edge represents connexin-26 KO/hzt (r, 3.5 µm; l, 18.5 µm); solid green, connexin-26 KO (r, 3.5 µm; l, 18.09 µm; Zhu et al., 2013). Solid red represents connexin-26 KO (C_{LW} is the same as wild type; Zhu et al., 2015), and solid black represents hzt/prestin KO (r and l = 84% of wild type; Cheatham et al., 2005). The two arrows on the right represent the range of the ex vivo (Johnson et al., 2011; purple arrow) and in vivo (Cody and Russell, 1987; Dallos, 1985; Russell and Kössl, 1992; pink arrow) membrane potential of OHCs at 37°C. The dashed lines are described in panel a.

determined the pseudo-minimum at the depolarizing voltage, V_d to be 0.033 V and determined an unconstrained linear fit of −0.401 (fit not shown; adjusted R^2 = 0.95). Also shown on the plot are the data determined in the presence of XE991, where V_d is at 0.05 V with an unconstrained linear fit of −0.37 (fit not shown; adjusted R^2 = 0.87). These data obtained by voltage clamping OHCs from albino and normal guinea pigs show that $V_{0.5}$ is related to ΔV_{min}^{exp}, as predicted by Eq. 3a.

Data reported from other rodents also align with the relationship observed for OHCs from guinea pigs. Measurements made with OHCs from young albino rats (Mahendrasingam et al., 2010) are shown in Fig. 3 a (open red diamonds). In this case, parameters were determined upon fitting the data to a two-state Boltzmann function (Mahendrasingam et al., 2010). We determined C_{LW} by two methods: (1) from the length (l) and radius (r) of the cells and by making use of $C_{LW} = 2\pi r(l - r) \times 0.01$, where we found it to be 8.9 and 3.3 pF for apical and basal originating cells; and (2) by use of equation Eq. 8a, where we estimated the lateral membrane capacitance to be 9.56 (apical cells) and 3.55 pF (basal cells). We used the average of these values to calculate ΔV_{min}^{exp}. Data from five studies that examined OHCs isolated from wild type mice (Cheatham et al., 2005; Homma et al., 2013; Yamashita et al., 2012; Zhu et al., 2013, 2015) are also plotted in Fig. 3 a. These data are not partitioned based on positional polarity of the cells (frequency position) within the cochlea; one average value is determined for each electrical parameter. Four of the five values lie within the data observed for the high-frequency guinea pig cells, with one (red square) exhibiting a value that is more hyperpolarized for the reported ΔV_{min}^{exp}. This shows that $V_{0.5}$ is related to ΔV_{min}^{exp}, as predicted by Eq. 3a for OHCs from guinea pigs, rats, and mice.

Comparison of the experimental results from engineered mice with Eq. 3a

Further evidence to show that $V_{0.5}$ is related to ΔV_{min}^{exp} is provided when key proteins were changed by knockout (KO) or knockin (KI) experiments. Zhao and colleagues engineered mice to KO connexin 26 and reported a hyperpolarizing shift for $V_{0.5}$. Close examination of this data shows an average charge increase from 0.72 to 0.8 pC for cells extracted from homozygotes compared with wild type animals. Although they reported that this increase in charge was not statistically significant, we note this increase is noticeable in their data (see Fig. 6 A of Zhu et al. (2013)) and correlates with their reported increase in prestin-gene expression. We used the mean reported length of the cell and assumed the radius to be 3.5 µm to determine a mean lateral wall capacitance of 3.58, 3.4, and 3.49 pF for cells from wild type, homozygote, and heterozygote. ΔV_{min}^{exp} was calculated and is shown in Fig. 3 c, where the points lie within the range observed for the wild type rodents (solid green squares). For a second study with another mouse, Zhu et al. (2015) observed a depolarizing shift when connexin 26 was conditionally knocked out, albeit they also observed a reduced voltage sensitivity and reduced endocochlear potential, where the latter is expected to limit the hearing thresholds of the animal independent of the charge displacement reaction. These data are also shown (Fig. 3 c, solid red square).

Data obtained from cells extracted from a mouse that was modified to decrease the production of prestin (neo-neo mouse) exhibits a lower ΔV_{min}^{exp}, increased voltage sensitivity, and a small depolarizing shift (<10 mV) of $V_{0.5}$ relative to the wild type. The

Downloaded from http://rupress.org/jgp/article-pdf/152/7/e201912447/1801126/jgp_201912447.pdf by guest on 09 February 2026

data are also shown in Fig. 3 c (magenta), where the measured values fall beyond that observed for cells from wild type rodents (Yamashita et al., 2012). In this same study, the results obtained from cells from the heterozygote (neo/prestin KO) mouse are plotted and also fall beyond that observed for cells from wild type rodents (Yamashita et al., 2012). In these cases, the ΔV_{min}^{exp} is 57% (neo/prestin KO) and 35% (neo-neo mouse) lower, while the $V_{0.5}$ is slightly depolarized or about the same for both cases. This shows that, for cells extracted from the neo-neo mouse, this manipulation of lowering the number of sensors has a (relatively) small effect on $V_{0.5}$, implying that the intrinsic properties of the sensor are similar to the wild type. In contrast, OHCs from the KI 499 mouse (cyan) lie well beyond the rest of the data (Homma et al., 2013); there is a significant positive shift in $V_{0.5}$ and a 10-fold reduction of ΔV_{min}^{exp}. Like the neo-neo variant, data obtained from OHCs from the heterozygote 499 mice also exhibit a 50% decrease in ΔV_{min}^{exp}, with a slightly depolarized $V_{0.5}$ (Fig. 3 c) and reduced (10% lower) voltage sensitivity. Data obtained from the C1 KI mouse (gray) exhibited similar charge density to the wild type, but with a significantly negative $V_{0.5}$ and decreased voltage sensitivity (Gao et al., 2007). Finally, the data obtained from cells extracted from the heterozygote prestin KO mouse (black) are comparable to the wild type, where the authors suggested that the number density of prestin molecules increased to compensate for the lack of one wild type prestin gene (Cheatham et al., 2005). This result was also different from the first prestin KO study, in which electromotility (displacement charge not measured) was reduced twofold in cells extracted from the heterozygote mice (Liberman et al., 2002).

Asymmetry of *C* versus *V* function

The model specifies that the capacitance where voltage sensors reside is identical in the two pseudo-minimum states (Kim and Warshel, 2016). This assumption is not strictly valid for the voltage sensors found in OHCs (Santos-Sacchi and Navarrete, 2002). For our data, the membrane capacitance observed in the hyperpolarized region is 2.76 ± 1.32 pF (number of observations, 62) more than the capacitance measured at positive voltages (Fig. S5). We estimated the linear capacitance at the negative voltage, C_L^n, and calculated the net difference (ΔC) by comparing it with that determined at positive potentials. We then determined the capacitance of the lateral membrane at negative potentials, C_{LW}^n, by adding this difference onto the C_{LW} determined with Eq. 8a. In some observations, C_L^n could not be estimated, as the capacitance had not reached its plateau (hyperpolarized) value. When $\Delta C > 5$ pF, we discounted the measurements and report a ΔC of 2.87 (±1.27) and 2.53 (±1.47) pF for cells from apical and basal regions. This amounts to a 13% (apical) and 21% (basal) increase in the linear capacitance of the lateral membrane. We estimate the specific capacitance at this region to be 0.01106 ± 0.0016 pF/μm² (Fig. S5), with a change in the specific capacitance of ∼0.00156 pF/μm². We partitioned the data making use of C_{LW}^n (compare C_{LW}) and plotted it as a function of $V_{0.5}$ in Fig. 3 b. The data, when constrained to fit Eq. 3a, exhibit an intercept of 0.02 V (dashed blue line), whereas the data when unconstrained exhibit a steeper slope with a value of −0.66 and an intercept of 0.046 V (dashed black line). Therefore, we conclude upon fitting the guinea pig data unconstrained to a linear function (Fig. 3) that the mean value for all unconstrained slopes is approximately −0.48 (i.e., mean of slopes −0.4, −0.37, and −0.66) which is approximately −0.5.

More than one configurational state of the prestin sensor when hyperpolarized

We calculated with Eq. 3 V_h and V_d for prestin sensors on the lateral membrane of rodents and found that V_h increases monotonically by threefold while V_d remains approximately constant (Fig. 4 a). The hyperpolarized state of the sensor becomes less energetically stable (more positive) as V_h increases, while the depolarized state of the sensor remains at the same level. Again, this suggests that there is more than one configurational state of the sensors when hyperpolarized. We next characterized the states with the data obtained with linear capacitance measured at positive potentials (Fig. 3 a and Fig. S4) and calculated the mean charge moved, q; the mean area of the sensor, A_{mean}; the mean capacitance of the membrane where a sensor resides, $C_{L,eq}$; and the mean $V_{0.5}$ of the prestin sensor on the lateral membrane.

Determine q, A_{mean}, $C_{L,eq}$, and $V_{0.5}$ for one prestin sensor in lateral membrane

We found that δ is relatively constant at approximately −0.5 when the reaction is midway (Fig. 3) and first assumed that the charge (ne_o) is displaced along the entire fraction of the dielectric at the end of the reaction, i.e., $\delta \equiv 1$, and calculated the mean surface area, A_{mean} that one voltage sensor occupies in the lateral membrane. We did this to establish that the value is reasonable, given the size of the topology model of prestin determined with the I-TASSER server (Roy et al., 2010; Yang et al., 2015; Zhang, 2008; Fig. 4 b). We found for our experimental data that the limiting membrane area for the wild type voltage sensor was 51 to 121 nm², which we calculated from the experimental values of ΔV_{min}^{exp} and a specific capacitance of 0.0095 pF/μm² (Fig. S5). Similar values were calculated for sensors from wild type rats and mice (Fig. 4 c). Examination of this data shows $|V_{0.5}| \propto [A_{mean}]^{-1.5}$. Our predicted transmembrane domain of prestin (Fig. 4 b) exhibits a radius of 3.4 and 3.15 nm when viewed from the cytoplasmic and extracellular sides, respectively. The maximum area of this domain is ∼36.3 nm², slightly larger than that obtained for the fumarate bacterial transporter, SLC26Dg (Geertsma et al., 2015), at 34.2 nm² (Fig. 4 c). As expected, the areas for this template and our predictive model are less than the area calculated from the electrophysiological data, because membrane proteins are usually present at concentrations of 1–2% in membranes. The model that fits into a symmetrical membrane of thickness 2.78 nm (Fig. S6) provides a limit for the membrane-spanning sensor area and a limit for $V_{0.5}$ at −0.177 V, albeit in one conformation and for one monomer.

Likewise, $C_{L,eq}$ is calculated with $ne_o/\Delta V_{min}^{exp}$ and found to exhibit two limits. The first is 0.584 (±0.065) aF, which is apparent at a mean $V_{0.5}$ less than −0.06 V and increases monotonically to 1.07 (±0.038) aF as $V_{0.5}$ increases to −0.03 V (Fig. 4 d). This change in the capacitance is almost exactly twofold. The capacitance for our model sensor, where we assume the same

Downloaded from http://rupress.org/jgp/article-pdf/152/7/e201912447/1801126/jgp_201912447.pdf by guest on 09 February 2026

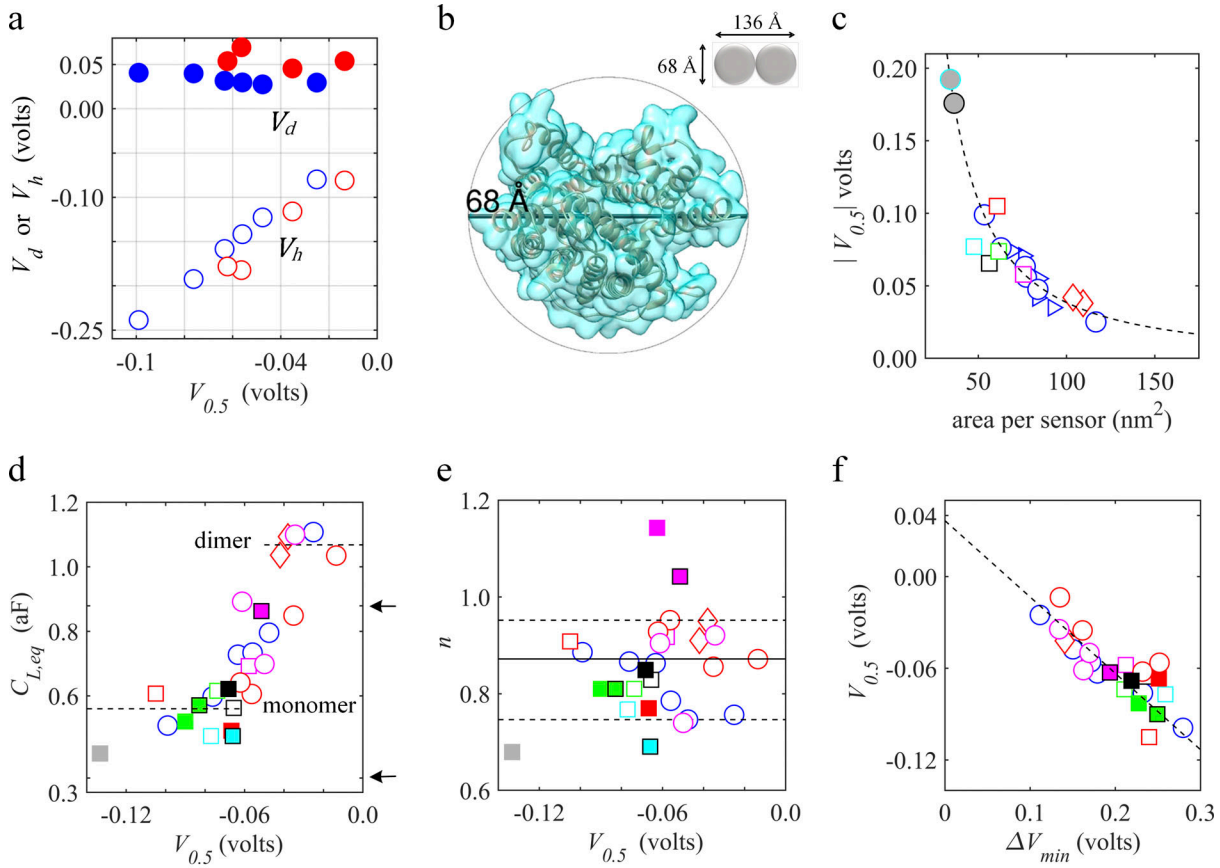

Figure 4. **Evidence for two hyperpolarized states of the prestin sensor. (a)** Calculated pseudo-minima determined from data (guinea pig) shown in Fig. 3 a, where circles represent XE991 added (red) and not added (blue) to the bath. Open and closed symbols represent the pseudo-minima of the hyperpolarized and depolarized states, respectively. **(b)** I-TASSER 3D predicted structure of prestin (guinea pig transmembrane domain). Tan and cyan colors depict the backbone and space-filling model of the transmembrane domain. The structure is viewed from the cytoplasmic side. The diameter of the overlaid circle (68 Å) represents the distance between two points furthest apart on the space-filling model. The inset shows the dimension of a dimer in the same orientation. **(c)** Mean membrane area of wild type sensor. The filled gray circle with a black border represents the mean membrane area of the predicted model (shown in b), and the gray circle with cyan border represents the mean area of SLC26Dg homologue (PDB accession no. 5DA0). The dashed line is the power relationship $|V_{0.5}| \cong [38.5A_{mean}]^{-1.15}$ obtained from OHCs from guinea pig (open blue circles). **(d)** The capacitance of the membrane where one sensor resides, calculated assuming the reaction ends at $\delta \equiv 1$; hence $z \equiv n$. Dashed lines represent the mean capacitance measured for a putative monomer and dimer. Arrows indicate capacitance calculated for the homology model of transmembrane prestin (see b). **(e)** Charge of the sensor for wild type and engineered animals. The mean value for the wild type sensor (solid line) and minimum and maximum values (dashed lines). **(f)** The charge density of the sensor from rodents after correcting for lower number density for cells from heterozygote animals. The dashed line is the fit of data from all rodents with and without XE991 in the bath to Eq. 3a with intercept, V_d 0.037 V (adjusted R^2, 0.538). Symbols in c–f are described in Fig. 3, a and c, except open magenta circles, which represent experiments performed with OHCs from the normal mammalian phenotype in the presence of XE991 in the bath with 10 mM chloride and 133 mM glutamate within the patch pipette.

specific capacitance (0.095 pF/μm^2), is 0.34 aF (monomer) and 0.878 aF (dimer; black arrows, Fig. 4 d). The charge is shown as a function of $V_{0.5}$ in Fig. 4 e. The magnitude of the charge is similar for all sensors at 0.873 ± 0.0577 (maximum 0.952; minimum 0.767; $C_{L,eq}$ 0.584 aF) and 0.872 ± 0.083 (maximum 0.95; minimum 0.756; $C_{L,eq}$ 1.07 aF) with a range for all wild type at 0.859 ± 0.066 (maximum 0.952; minimum 0.746). Corresponding data for sensors from KI 499 heterozygote mice (solid cyan black edge), neo-neo mice (solid magenta black edge), and C1 KI (gray square) are also shown in Fig. 4 d, with the latter positioned beyond the wild type sensor region. The sensors from cells of heterozygote neo-neo mice exhibited similar $V_{0.5}$ and similar q values to native cells. Their decreased density arises from a lower number of sensors within the same (approximate) area of the lateral membrane, and we corrected $C_{L,eq}$ by multiplying by the ratio of charge density determined for heterozygotes relative to that determined for wild type cells. Consider that such a correction would be needed with prestin-transfected cells, as the charge density measured (even with inducible cell lines) is always much less (e.g., ΔV_{min}^{exp} 0.0206 V; Bian et al., 2010) than that observed for native cells, but the electrical characteristics of prestin (e.g., 0.76 e_o and $V_{0.5}$ −0.077 V; Bian et al., 2010) are similar to those of native cells. The charge density is lower because significant regions of the plasma membrane of these cultured cells are devoid of sensors, and the two regions (sensor and sensorless) are indistinguishable experimentally.

The magnitude of ΔV_{min}, i.e., the equilibrium potential difference between two putative quasi-equilibrium states for

Downloaded from http://rupress.org/jgp/article-pdf/152/7/e201912447/1801126/jgp_201912447.pdf by guest on 09 February 2026

prestin sensors from the lateral membrane of all rodents (except for 499 KI and heterozygote 499, C1 KI and neo/prestin KO) is shown as a function of $V_{0.5}$ in Fig. 4 f, where we fitted all the data to Eq. 3a independent of chemical bath composition. An alternative limit to interpret the data of Fig. 3 is to assume that $C_{L,eq}$ is constant at some maximum measured value (e.g., $C_{L,eq} \equiv 1.098$ aF) and then calculate values for n and δ at the end of the reaction. Although we cannot discount this alternative limit, we suggest that the first approach is more appropriate, i.e., the reaction completes at δ ≈ 1 and the relationship (Figs. 3 and 4) is primarily the result of a change in $C_{L,eq}$ because it is illogical for δ to be 0.535 at the end of the reaction and ∼0.5 midway in the reaction (Fig. 3). (Note: $C_{L,eq} \equiv 1.098$ aF, the alternative approach when n is calculated with $\Delta V_{min}^{exp} C_{L,eq}/e_o$ and δ is calculated with Eq. 5 [n/z], finds 1.7 charges [maximum 1.92, minimum 1.44] moving a fraction of the distance, δ = 0.535 [maximum 0.63, minimum 0.432]).

Discussion

Kinetic scheme

We present a kinetic scheme in Fig. 5 with two pathways for charge movement. Consider the reactant which we posit is a dimer and in a fully hyperpolarized state (R_2). Upon applying a positive potential, each monomer of the dimer transfers charge ($n \equiv 0.86e_o$) simultaneously to produce the depolarized product (P_2). This interacts in a voltage-independent step (equilibrium constant, K_2) to form the depolarized dimer that we posit represents the contracted state of the molecule ($P - P$). We suggest that the latter is the detected stable depolarized state (Fig. 4 a). This mechanism is similar to that proposed for ion channels, where monomers behave independently and synchronously (Zagotta et al., 1994). The second pathway is where each monomer of the hyperpolarized dimer displaces $-0.86e_o$ and $+0.86e_o$ charges in a voltage-independent step. This intermediate transition ($T - T$) then undergoes a voltage-dependent transition in which $+0.86e_o$ of charge is displaced across the membrane to produce the $P - P$ state. The monomers of a dimer act in a synchronous fashion. The net charge moved by the dimer during the reaction is $-0.86e_o + 0.86e_o + 0.86e_o$. This scheme provides two configurational states, R_2 and ($T - T$), of the sensor when hyperpolarized as suggested by data in Figs. 3 and 4. These data and analysis support the hypothesis that the sensor is a dimer (Bian et al., 2010; Detro-Dassen et al., 2008; Zheng et al., 2006).

The parameters determined for the pathways are found in Table 3. The $V_{0.5}$ associated with pathway 1 (K_1 and K_2) is −0.076 ± 0.014 (minimum −0.1; maximum −0.056) V. We calculate the activation energy barrier $\Delta G^{\S}$ at 2.68 $\kappa_B T$/monomer ($T \equiv$ 24°C, 1.58 kcal/mol of monomers) and 5.36 $\kappa_B T$/dimer (3.16 kcal/mol of dimers) with expression Eq. 7 and reorganization energy for charge transfer (K_1) for the wild type sensor at ∼3.95 $\kappa_B T$/monomer (2.33 kcal/mol of monomers) and 7.91 $\kappa_B T$/dimer (4.67 kcal/mol of dimers) with Eq. 6a. Note that the $\Delta G^{\S}$ ($V \equiv 0$) at ∼5.4 $\kappa_B T$ is the magnitude expected for a fast reaction (Delemotte et al., 2015; Sigg et al., 2003). Likewise, the $V_{0.5}$ associated with K_3 and K_4 is −0.031 V (± 0.007; minimum −0.043; maximum −0.013), where we calculate $\Delta G^{\S}$ of 1.2 $\kappa_B T$/dimer (0.7 kcal/mol of dimers) and reorganization energy at 2.16 $\kappa_B T$/dimer

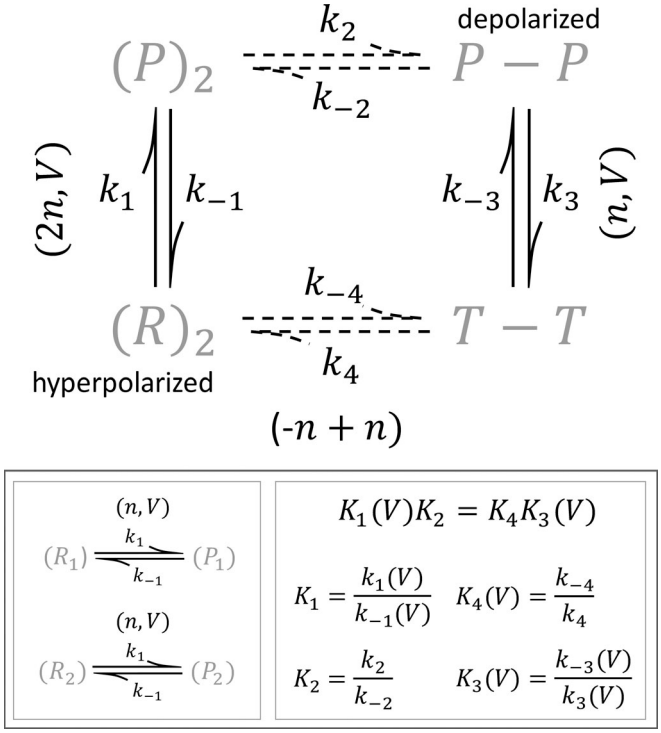

Figure 5. **Reaction scheme with two charge-displacement pathways.** The first pathway is a voltage-dependent reaction with a rate constant, k_1, and (R_2) is converted to (P_2), where each monomer acts independently and synchronously. This is followed by a reaction where monomers interact (rate constant, k_2) to produce the depolarized state $P - P$. The second pathway forms state $T - T$ by an electroneutral reaction (rate constant, k_{-3}), which is followed by a voltage-dependent reaction (rate constant, k_{-4}), where n charges are displaced by the dimer. The reverse rates are indicated for each step. The inset shows the reaction for step k_1 and the definition of the equilibrium constants. Solid arrows and dashed arrows represent voltage-dependent and -independent reactions.

(1.27 kcal/mol of dimers). This second pathway (K_3 and K_4) decreases the activation energy required for the voltage-dependent step significantly by making use of an electroneutral mechanism. It resembles most closely an anion-antiporter exchange mechanism proposed by Muallem and Ashmore (2006). They suggested that anions together with net positively charged residues move across the dielectric upon depolarization. The anion that is transferred then exchanges with 2 × monovalent anion at the extracellular side to produce a neutralized motif that is then

Table 3. **Parameters determined for pathways at $T \equiv$ 24°C (wild type)**

Parameter	$C_{L,eq}$ (aF)	$V_{0.5}$ (V)	z	$\Delta G^{\S}$ ($\kappa_B T$)	λ ($\kappa_B T$)
K_1 (V)	0.584 (0.065)	−0.076 (0.014)	0.859 (0.066)	2 × 2.68 (forward)	2 × 3.97
				2 × 0.125 (reverse)	
K_3 (V)	1.07 (0.038)	−0.031 (0.007)	0.859 (0.066)	1.19 (forward)	2.16
				0.145 (reverse)	

Downloaded from http://rupress.org/jgp/article-pdf/152/7/e201912447/1801126/jgp_201912447.pdf by guest on 09 February 2026

shuttled back to the intracellular side in a voltage-independent manner. Their scheme explained the concomitant decrease of Q_T^m with an increase of $V_{0.5}$ as intracellular [Cl^-] decreased (Oliver et al., 2001). In contrast, our hypothesis was deduced from experiments performed with ∼140–145 mM of intracellular chloride. When we performed experiments in 10 mM intracellular chloride with coion glutamate, results were similar to those observed at high concentrations of intracellular chloride (magenta circles in Fig. 4, d–f). However, it is probable that the putative negative charge originates from an anion, as there is evidence that prestin exhibits a nonselective anionic conductance (Bai et al., 2017), and transport of anions albeit weakly appears to be integral to the function of the protein (Mistrík et al., 2012; Schänzler and Fahlke, 2012). Our scheme also resembles some details of other models (Homma and Dallos, 2011; Song and Santos-Sacchi, 2013), one of which (Homma and Dallos, 2011) suggests there is one pathway with two voltage-dependent steps, while the other (Song and Santos-Sacchi, 2013) suggests there is one pathway with a voltage-dependent transition (e.g., K_4) that is followed by a voltage-independent transition (e.g., K_3) upon rapid anion binding to the sensor at the cytoplasmic side. Our data and analysis and the other models (Homma and Dallos, 2011; Muallem and Ashmore, 2006; Song and Santos-Sacchi, 2013) all suggest there are more than two stable states of the sensor.

This analysis also finds that the net displacement charge is positive, as suggested (Homma and Dallos, 2011; Muallem and Ashmore, 2006; Song and Santos-Sacchi, 2013). Of interest, we found the transmembrane domain of the topology model (Fig. 4 b) to conform to the positive inside rule observed for membrane proteins (von Heijne and Gavel, 1988). This would produce a potential difference across the membrane in the opposite sense of the plasma membrane (see below). In contrast, the ligand-free STAS domain (Pasqualetto et al., 2010) is predicted to be an extremely negatively charged domain at −16.3 (percent buried, <90) or −14 (percent buried, <25) charges, presumably ensuring the STAS is found within the cytoplasm and surrounded by positive counter ions (Table S4). Finally, the chemical component of the free energy change or the difference between two conformational states at $V \equiv 0$ is given by $\Delta G_{chem} = -RT\ln\left\{[K_1(V \equiv 0)]^2 K_2\right\}$, and we calculate ΔG_{chem} at 6.7 $\kappa_B T$ (3.96 kcal/mol; $\Delta G_{chem} = -RT\ln\left[(K_1)^2 K_2\right]$, which equals $-(0.860 \times e_o \times 2 \times -0.1)$), where we assume $V_{0.5}$ is constant and independent for $\Delta V_{min}^{exp} > 0.3$ V (Fig. 3 a and Fig. S4), and we take the minimum $V_{0.5}$ as the limit.

This analysis indicates that we detect two states. We calculate with Eq. 6b the predicted charge if only one of the states exists within the lateral membrane and compare these calculations with the experimental data to show that these two states cover the data range (Fig. 1, dashed red lines). We note that measurements that lie between the two limits represent cells with different mixtures of the two states of the sensors. Thus, we now suggest that charge density varies not necessarily by a different number density (Corbitt et al., 2012), but by different mixtures of the two putative states. Such mixtures will cause local variations in $V_{0.5}$ within the lateral membrane as reported (Santos-Sacchi, 2002), and likewise local variations in charge density (Corbitt et al., 2012), which is supported by nonuniform distribution of the OHC transmembrane potential (Ramamoorthy et al., 2013).

Physiological implications

These data (Figs. 3 and 4 and Table 3), when considered within a theoretical framework, suggest there is more than one pathway for charge displacement in the lateral membrane of OHCs. This multiplicity of pathways, if confirmed, implies there is diversity for both the reaction rate and the gain needed for sound amplification in vivo. This multiplicity would seem to be a reasonable biological strategy for a reaction that is critical for hearing. For example, we predict that the voltage-dependent rate at $V \equiv 0$ for pathway 2 (k_{-3}) is 64 × faster than pathway 1 (k_1), i.e., $e^{-1.2}/e^{-5.36}$, with the reverse rate for pathway 2 (k_3) marginally faster (10%) than the reverse rate for pathway 1 (k_{-1}), i.e., $e^{-0.145}/e^{-0.25}$. Likewise, for the engineered sensors, we calculate $\Delta G^{\S}$ (at $V \equiv 0$) for the sensors of the connexin 26 KO mouse with the mean forward (k_1) rates 60% slower than wild-type sensors $e^{-5.86}/e^{-5.36}$, with the mean reverse rate (k_{-1}) 10% faster than the wild type sensors ($C_{L,eq}$ 0.52 aF, $V_{0.5}$ −0.090 V, and z 0.81). Zhao and colleagues suggest that the hyperpolarizing shift observed (Figs. 3 c and 4, c–f, green squares; Zhu et al., 2013) is responsible for hearing loss in the connexin 26 KO mouse. However, we suggest the hearing loss is not primarily caused by electromotility, or more precisely charge movement, because the degree of hearing loss was significant and does not correlate with charge density or $V_{0.5}$ (Fig. S7). Likewise, the sensors from the C1 KI mouse exhibited forward rate (k_1) at $V \equiv 0$ that is 18% slower than the wild type ($e^{-7.1}/e^{-5.36}$), with the reverse rate for the C1 sensor almost barrierless (i.e., parentheses of Eq. 7 is very small $C_{L,eq}$, 0.41 aF, $V_{0.5}$ −0.133 V, and z 0.68). These animals exhibit hearing thresholds similar to the wild type animals except at low frequencies <5 kHz (Gao et al., 2007), where a hearing loss of ≤12 dB (Fig. S7) was reported. The 499 animal suffers a significant hearing loss (Dallos et al., 2008), which is readily apparent by the 10-fold reduction in the charge density and the significant positive $V_{0.5}$, even with iodide as the anion (Fig. 3 c; Homma et al., 2013). If we assume that the number density of sensors and the linear capacitance of lateral membrane is comparable to the wild type, then we calculate a $C_{L,eq}$ that is four to five times more than the wild type and calculate activation and deactivation barriers for forward (k_{-3}) and reverse (k_3) rates of 7.7 and 11 $\kappa_B T$, respectively ($C_{L,eq}$ 2.7 aF, $V_{0.5}$ 0.168 V, and z 0.51). This predicted increase in the deactivation energy $\Delta G^{\S}$ for the 499 sensors provides an energetic explanation for why this mutation impairs kinetics at frequencies >200 Hz (Homma et al., 2013). It also predicts that the depolarized state is more stable than the hyperpolarized state, which is the opposite of the wild type sensor.

Caveats associated with the model and data

Many of the assumptions implicit in the model are discussed in Kim and Warshel (2016), except the assumption that the membrane is symmetrical. This is relevant, as cell membranes are asymmetrical both chemically and when considering surface charge (Farrell et al., 2006). Considering the influence of the

Downloaded from http://rupress.org/jgp/article-pdf/152/7/e201912447/1801126/jgp_201912447.pdf by guest on 09 February 2026

surface charge, usually the inner leaflet exhibits a more negative surface charge than the outer leaflet, where this difference between the surface potentials can be written as

$$\Delta\psi_s = V_i(-d) - V - V_e(0), \quad (9a)$$

where $V_i(-d)$ is the potential at the surface of the internal leaflet, $V_e(0)$ is the potential at the external leaflet, V is the transmembrane potential, and $\psi_t = V_i(-d) - V_e(0)$, and equivalent to the voltage drop across the membrane (Farrell et al., 2006). At $V \equiv V_{0.5}$, the voltage drop across the membrane is then

$$\Delta\psi_s \cong \psi_t - V_{0.5}, \quad (9b)$$

and for a change in $\Delta\psi_t$ then

$$\Delta\Delta\psi_s \cong \Delta\psi_t - \Delta V_{0.5}. \quad (9c)$$

When $\Delta\psi_t$ becomes more negative, $V_{0.5}$ will shift in a positive direction, and when $\Delta\psi_t$ becomes more positive, $V_{0.5}$ will shift in a negative direction. Such shifts, as a result of changes in ψ_t are described for membrane proteins (González-Pérez et al., 2010) including prestin (Kuwabara et al., 2018). Thus, any manipulation that changes ψ_t (without also affecting $n\delta$) will shift $V_{0.5}$ according to Eq. 9. For example, one natural variation in $\Delta\psi_s$ is the degree of phosphorylation at residue S238 (Deák et al., 2005; Frolenkov et al., 2001). The effect of $\Delta\psi_s$ in this case, would be to shift both pseudo-equilibrium potentials (V_d and V_h) to higher voltages. This illustrates that a change in the potential drop across the membrane as a result of depletion or excess charge at the surface (provided it is within a Debye length) can affect $V_{0.5}$ and contribute to the experimental variance. Indeed, the main findings required averaging the results from many cells to account for this variance and that associated with Q_T^M and C_{LW} (Figs. 2, 3, and 4). Clearly, it would be useful to normalize $V_{0.5}$ measured in cells based on $\Delta\psi_s$ of the membrane. It would also be useful to develop models for the case when sensors are placed within asymmetrical membranes.

As stated, the expressions derived to calculate the magnitude of the energy barriers (Table 3) may not include the energy needed to move the charge (Kim and Warshel, 2016). Also, reaction rates depend on the diffusive-motion of the sensor in the membrane, the electrical term (Kramers, 1940; Sigg et al., 2003), and for prestin, membrane tension (Adachi and Iwasa, 1999; Kakehata and Santos-Sacchi, 1995). As mentioned, reported high-resolution measurements of the rate are sparse and only documented the limiting reaction rate (Gale and Ashmore, 1997). More data are needed to better discern the rate laws. This could be accomplished by measuring rates of charge movement, rates of membrane displacement, or rates of force production at high temporal resolution concomitantly with membrane potential, and in conjunction with performing experiments in silico (Kasimova et al., 2018; Kim and Warshel, 2015, 2016; Machtens et al., 2017; Roux, 2008) with model sensors in asymmetric membranes.

Our experiments were performed under nonphysiological conditions (e.g., solutions with ion channel blockers and nonphysiological buffers), so it is not expected that $V_{0.5}$ determined ex vivo should coincide with in vivo measurements of the silent or resting membrane potential (Cody and Russell, 1987; Dallos, 1985; Russell and Kössl, 1992). We do, however, find that the membrane potential measured in cells in the basal region at −72 mV (range −70 to −105 mV; Cody and Russell, 1987) and −64 mV (range −58 to −70 mV; Russell and Kössl, 1992) are comparable with our ex vivo measurements of $V_{0.5}$ at −72 mV (range −47 to −105 mV) after correcting to physiological temperature (Meltzer and Santos-Sacchi, 2001; Fig. 4 d, bottom arrow). In contrast, the resting membrane potential was −71 mV (range −75 to −56 mV) for turn 3 cells (Dallos, 1985), while the central tendency of $V_{0.5}$ is 30 mV more depolarized at −40 (± 0.022) mV after correcting for temperature (Meltzer and Santos-Sacchi, 2001). These data are closer to the ex vivo resting membrane potential measurements reported by Johnson et al. (2011).

Finally, it is well known that OHCs cannot survive for long times after extraction from the cochlea. However, we did not find a correlation with the magnitude of the electrical parameters and time of the recording relative to the lifetime boundary of the animal (Table S1). Indeed, our data and this analysis are consistent with other rodent data, including recordings from OHCs of mice that were made after a shorter time (~20–30 min) relative to the lifetime boundary of the animal (e.g., the data represented with cyan [Homma et al., 2013] in Fig. 3). We note that this rundown impacts all ex vivo preparations (Cheatham et al., 2005; Homma et al., 2013; Mahendrasingam et al., 2010; Yamashita et al., 2012; Zhu et al., 2013, 2015), and even if our main finding, i.e., Figs. 3, 4, and 5, results in part because of loss of physiology gradients, our analysis shows that prestin can form two stable hyperpolarized states. Further work is required to establish whether they are relevant physiologically.

Acknowledgments

Richard W. Aldrich served as guest editor.

We thank Varun K.A. Sreenivasan, PhD, for help performing whole-cell patch-clamp experiments in XE991, and Kazuaki Homma, PhD, and Mary A. Cheatham, PhD, for providing the data from the C1 mouse.

This work was funded by the National Institute on Deafness and Other Communication Disorders (R01DC00354 and R01DC00354-S1) and National Institutes of Health–U.S. National Library of Medicine.

The authors declare no competing financial interests.

Author contributions: Conceptualization: B. Farrell and W.E. Brownell; Formal Analysis: B. Farrell; Funding Acquisition: B. Farrell and W.E. Brownell; Investigation: V. Rajasekharan and B.L. Skidmore; Methodology: B.L. Skidmore; Software: B. Farrell; Validation: B. Farrell; Writing–original and revised drafts: B. Farrell; Editing: B. Farrell, B.L. Skidmore, W.E. Brownell, and V. Rajasekharan.

Submitted: 15 July 2019
Accepted: 18 March 2020

References

Adachi, M., and K.H. Iwasa. 1999. Electrically driven motor in the outer hair cell: effect of a mechanical constraint. *Proc. Natl. Acad. Sci. USA.* 96:7244–7249.

Al-Sabi, A., S.K. Kaza, J.O. Dolly, and J. Wang. 2013. Pharmacological characteristics of Kv1.1- and Kv1.2-containing channels are influenced by the stoichiometry and positioning of their α subunits. *Biochem. J.* 454:101–108.

Downloaded from http://rupress.org/jgp/article-pdf/152/7/e201912447/1801126/jgp_201912447.pdf by guest on 09 February 2026

Bai, J.P., I. Moeini-Naghani, S. Zhong, F.Y. Li, S. Bian, F.J. Sigworth, J. Santos-Sacchi, and D. Navaratnam. 2017. Current carried by the Slc26 family member prestin does not flow through the transporter pathway. *Sci. Rep.* 7:46619.

Bai, J.P., A. Surguchev, S. Montoya, P.S. Aronson, J. Santos-Sacchi, and D. Navaratnam. 2009. Prestin's anion transport and voltage-sensing capabilities are independent. *Biophys. J.* 96:3179–3186.

Bian, S., B.W. Koo, S. Kelleher, J. Santos-Sacchi, and D.S. Navaratnam. 2010. A highly expressing Tet-inducible cell line recapitulates in situ developmental changes in prestin's Boltzmann characteristics and reveals early maturational events. *Am. J. Physiol. Cell Physiol.* 299:C828–C835.

Brownell, W.E., C.R. Bader, D. Bertrand, and Y. de Ribaupierre. 1985. Evoked mechanical responses of isolated cochlear outer hair cells. *Science.* 227: 194–196.

Chakrapani, S., and A. Auerbach. 2005. A speed limit for conformational change of an allosteric membrane protein. *Proc. Natl. Acad. Sci. USA.* 102: 87–92.

Cheatham, M.A., J. Zheng, K.H. Huynh, G.G. Du, J. Gao, J. Zuo, E. Navarrete, and P. Dallos. 2005. Cochlear function in mice with only one copy of the prestin gene. *J. Physiol.* 569:229–241.

Chowdhury, S., and B. Chanda. 2012. Estimating the voltage-dependent free energy change of ion channels using the median voltage for activation. *J. Gen. Physiol.* 139:3–17.

Cody, A.R., and I.J. Russell. 1987. The response of hair cells in the basal turn of the guinea-pig cochlea to tones. *J. Physiol.* 383:551–569.

Cooper, N.P., A. Vavakou, and M. van der Heijden. 2018. Vibration hotspots reveal longitudinal funneling of sound-evoked motion in the mammalian cochlea. *Nat. Commun.* 9:3054.

Corbitt, C., F. Farinelli, W.E. Brownell, and B. Farrell. 2012. Tonotopic relationships reveal the charge density varies along the lateral wall of outer hair cells. *Biophys. J.* 102:2715–2724.

Dallos, P.. 1985. Response characteristics of mammalian cochlear hair cells. *J. Neurosci.* 5:1591–1608.

Dallos, P., X. Wu, M.A. Cheatham, J. Gao, J. Zheng, C.T. Anderson, S. Jia, X. Wang, W.H. Cheng, S. Sengupta, et al. 2008. Prestin-based outer hair cell motility is necessary for mammalian cochlear amplification. *Neuron.* 58:333–339.

Deák, L., J. Zheng, A. Orem, G.G. Du, S. Aguiñaga, K. Matsuda, and P. Dallos. 2005. Effects of cyclic nucleotides on the function of prestin. *J. Physiol.* 563:483–496.

Delemotte, L., M.A. Kasimova, M.L. Klein, M. Tarek, and V. Carnevale. 2015. Free-energy landscape of ion-channel voltage-sensor-domain activation. *Proc. Natl. Acad. Sci. USA.* 112:124–129.

Detro-Dassen, S., M. Schänzler, H. Lauks, I. Martin, S.M. zu Berstenhorst, D. Nothmann, D. Torres-Salazar, P. Hidalgo, G. Schmalzing, and C. Fahlke. 2008. Conserved dimeric subunit stoichiometry of SLC26 multifunctional anion exchangers. *J. Biol. Chem.* 283:4177–4188.

Dolinsky, T.J., J.E. Nielsen, J.A. McCammon, and N.A. Baker. 2004. PDB2PQR: an automated pipeline for the setup of Poisson-Boltzmann electrostatics calculations. *Nucleic Acids Res.* 32:W665–W667.

Dong, W., and E.S. Olson. 2013. Detection of cochlear amplification and its activation. *Biophys. J.* 105:1067–1078.

Farrell, B., and J. Bengtson. 2019. Scientist and data architect collaborate to curate and archive an inner ear electrophysiology data collection. *PLoS One.* 14. e0223984.

Farrell, B., C. Do Shope, and W.E. Brownell. 2006. Voltage-dependent capacitance of human embryonic kidney cells. *Phys. Rev. E Stat. Nonlin. Soft Matter Phys.* 73. 041930.

Forge, A.. 1991. Structural features of the lateral walls in mammalian cochlear outer hair cells. *Cell Tissue Res.* 265:473–483.

Frank, G., W. Hemmert, and A.W. Gummer. 1999. Limiting dynamics of high-frequency electromechanical transduction of outer hair cells. *Proc. Natl. Acad. Sci. USA.* 96:4420–4425.

Frolenkov, G.I., F. Mammano, and B. Kachar. 2001. Action of 2,3-butanedione monoxime on capacitance and electromotility of guinea-pig cochlear outer hair cells. *J. Physiol.* 531:667–676.

Gale, J.E., and J.F. Ashmore. 1997. An intrinsic frequency limit to the cochlear amplifier. *Nature.* 389:63–66.

Gao, J., X. Wang, X. Wu, S. Aguinaga, K. Huynh, S. Jia, K. Matsuda, M. Patel, J. Zheng, M. Cheatham, et al. 2007. Prestin-based outer hair cell electromotility in knockin mice does not appear to adjust the operating point of a cilia-based amplifier. *Proc. Natl. Acad. Sci. USA.* 104: 12542–12547.

Geertsma, E.R., Y.N. Chang, F.R. Shaik, Y. Neldner, E. Pardon, J. Steyaert, and R. Dutzler. 2015. Structure of a prokaryotic fumarate transporter reveals the architecture of the SLC26 family. *Nat. Struct. Mol. Biol.* 22: 803–808.

González-Pérez, V., K. Stack, K. Boric, and D. Naranjo. 2010. Reduced voltage sensitivity in a K+-channel voltage sensor by electric field remodeling. *Proc. Natl. Acad. Sci. USA.* 107:5178–5183.

Gorbunov, D., M. Sturlese, F. Nies, M. Kluge, M. Bellanda, R. Battistutta, and D. Oliver. 2014. Molecular architecture and the structural basis for anion interaction in prestin and SLC26 transporters. *Nat. Commun.* 5: 3622.

Hallworth, R., and M.G. Nichols. 2012. Prestin in HEK cells is an obligate tetramer. *J. Neurophysiol.* 107:5–11.

Heffner, R.S., G. Koay, and H.E. Heffner. 2001. Audiograms of five species of rodents: implications for the evolution of hearing and the perception of pitch. *Hear. Res.* 157:138–152.

Holley, M.C., and J.F. Ashmore. 1990. Spectrin, actin and the structure of the cortical lattice in mammalian cochlear outer hair cells. *J. Cell Sci.* 96: 283–291.

Holley, M.C., F. Kalinec, and B. Kachar. 1992. Structure of the cortical cytoskeleton in mammalian outer hair cells. *J. Cell Sci.* 102:569–580.

Homma, K., and P. Dallos. 2011. Evidence that prestin has at least two voltage-dependent steps. *J. Biol. Chem.* 286:2297–2307.

Homma, K., C. Duan, J. Zheng, M.A. Cheatham, and P. Dallos. 2013. The V499G/Y501H mutation impairs fast motor kinetics of prestin and has significance for defining functional independence of individual prestin subunits. *J. Biol. Chem.* 288:2452–2463.

Iwasa, K.H., and M. Adachi. 1997. Force generation in the outer hair cell of the cochlea. *Biophys. J.* 73:546–555.

Johnson, S.L., M. Beurg, W. Marcotti, and R. Fettiplace. 2011. Prestin-driven cochlear amplification is not limited by the outer hair cell membrane time constant. *Neuron.* 70:1143–1154.

Joshi, H.S., D.J. Watson, and A.P. Labhsetwar. 1973. Ovarian secretion of oestradiol, oestrone, 20-dihydroprogesterone and progesterone during the oestrous cycle of the guinea-pig. *J. Reprod. Fertil.* 35:177–181.

Kakehata, S., and J. Santos-Sacchi. 1995. Membrane tension directly shifts voltage dependence of outer hair cell motility and associated gating charge. *Biophys. J.* 68:2190–2197.

Kasimova, M.A., E. Lindahl, and L. Delemotte. 2018. Determining the molecular basis of voltage sensitivity in membrane proteins. *J. Gen. Physiol.* 150:1444–1458.

Keiler, S., and C.P. Richter. 2001. Cochlear dimensions obtained in hemicochleae of four different strains of mice: CBA/CaJ, 129/CD1, 129/SvEv and C57BL/6J. *Hear. Res.* 162:91–104.

Kim, I., and A. Warshel. 2015. Equilibrium fluctuation relations for voltage coupling in membrane proteins. *Biochim. Biophys. Acta.* 1848(11 Pt A): 2985–2997.

Kim, I., and A. Warshel. 2016. A Microscopic Capacitor Model of Voltage Coupling in Membrane Proteins: Gating Charge Fluctuations in Ci-VSD. *J. Phys. Chem. B.* 120:418–432.

Kramers, H.A.. 1940. Brownian motion in a field of force and the diffusion model of chemical reactions. *Physica.* 7:284–304.

Kuwabara, M.F., K. Wasano, S. Takahashi, J. Bodner, T. Komori, S. Uemura, J. Zheng, T. Shima, and K. Homma. 2018. The extracellular loop of pendrin and prestin modulates their voltage-sensing property. *J. Biol. Chem.* 293:9970–9980.

Legendre, K., S. Safieddine, P. Küssel-Andermann, C. Petit, and A. El-Amraoui. 2008. alphaII-betaV spectrin bridges the plasma membrane and cortical lattice in the lateral wall of the auditory outer hair cells. *J. Cell Sci.* 121:3347–3356.

Liberman, M.C., J. Gao, D.Z. He, X. Wu, S. Jia, and J. Zuo. 2002. Prestin is required for electromotility of the outer hair cell and for the cochlear amplifier. *Nature.* 419:300–304.

Liu, X.Z., X.M. Ouyang, X.J. Xia, J. Zheng, A. Pandya, F. Li, L.L. Du, K.O. Welch, C. Petit, R.J. Smith, et al. 2003. Prestin, a cochlear motor protein, is defective in non-syndromic hearing loss. *Hum. Mol. Genet.* 12: 1155–1162.

Lomize, M.A., I.D. Pogozheva, H. Joo, H.I. Mosberg, and A.L. Lomize. 2012. OPM database and PPM web server: resources for positioning of proteins in membranes. *Nucleic Acids Res.* 40:D370–D376.

Machtens, J.P., R. Briones, C. Alleva, B.L. de Groot, and C. Fahlke. 2017. Gating Charge Calculations by Computational Electrophysiology Simulations. *Biophys. J.* 112:1396–1405.

Mahendrasingam, S., M. Beurg, R. Fettiplace, and C.M. Hackney. 2010. The ultrastructural distribution of prestin in outer hair cells: a post-embedding immunogold investigation of low-frequency and high-frequency regions of the rat cochlea. *Eur. J. Neurosci.* 31:1595–1605.

Downloaded from http://rupress.org/jgp/article-pdf/152/7/e201912447/1801126/jgp_201912447.pdf by guest on 09 February 2026

Matsuda, K., J. Zheng, G.G. Du, N. Klöcker, L.D. Madison, and P. Dallos. 2004. N-linked glycosylation sites of the motor protein prestin: effects on membrane targeting and electrophysiological function. *J. Neurochem.* 89:928–938.

Meltzer, J., and J. Santos-Sacchi. 2001. Temperature dependence of nonlinear capacitance in human embryonic kidney cells transfected with prestin, the outer hair cell motor protein. *Neurosci. Lett.* 313:141–144.

Mistrík, P., N. Daudet, K. Morandell, and J.F. Ashmore. 2012. Mammalian prestin is a weak Cl^-/HCO_3^- electrogenic antiporter. *J. Physiol.* 590:5597–5610.

Muallem, D., and J. Ashmore. 2006. An anion antiporter model of prestin, the outer hair cell motor protein. *Biophys. J.* 90:4035–4045.

Müller, M., K. von Hünerbein, S. Hoidis, and J.W. Smolders. 2005. A physiological place-frequency map of the cochlea in the CBA/J mouse. *Hear. Res.* 202:63–73.

Nakagawa, T., J.S. Oghalai, P. Saggau, R.D. Rabbitt, and W.E. Brownell. 2006. Photometric recording of transmembrane potential in outer hair cells. *J. Neural Eng.* 3:79–86.

Oliver, D., D.Z. He, N. Klöcker, J. Ludwig, U. Schulte, S. Waldegger, J.P. Ruppersberg, P. Dallos, and B. Fakler. 2001. Intracellular anions as the voltage sensor of prestin, the outer hair cell motor protein. *Science.* 292:2340–2343.

Olsson, M.H., C.R. Søndergaard, M. Rostkowski, and J.H. Jensen. 2011. PROPKA3: Consistent Treatment of Internal and Surface Residues in Empirical pKa Predictions. *J. Chem. Theory Comput.* 7:525–537.

Pasqualetto, E., R. Aiello, L. Gesiot, G. Bonetto, M. Bellanda, and R. Battistutta. 2010. Structure of the cytosolic portion of the motor protein prestin and functional role of the STAS domain in SLC26/SulP anion transporters. *J. Mol. Biol.* 400:448–462.

Patuzzi, R.B., G.K. Yates, and B.M. Johnstone. 1989. Outer hair cell receptor current and sensorineural hearing loss. *Hear. Res.* 42:47–72.

Pettersen, E.F., T.D. Goddard, C.C. Huang, G.S. Couch, D.M. Greenblatt, E.C. Meng, and T.E. Ferrin. 2004. UCSF Chimera–a visualization system for exploratory research and analysis. *J. Comput. Chem.* 25:1605–1612.

Pujol, R., M. Lenoir, S. Ladrech, F. Tribillac, and G. Rebillard. 1992. Correlation between the length of outer hair cells and the frequency coding of the cochlea. *Auditory Physiology and Perception.* Y. Cazals, L. Demany, and K.C. Horner, editors. 45–52.

Rabbitt, R.D., S. Clifford, K.D. Breneman, B. Farrell, and W.E. Brownell. 2009. Power efficiency of outer hair cell somatic electromotility. *PLOS Comput. Biol.* 5. e1000444.

Rajagopalan, L., J.N. Greeson, A. Xia, H. Liu, A. Sturm, R.M. Raphael, A.L. Davidson, J.S. Oghalai, F.A. Pereira, and W.E. Brownell. 2007. Tuning of the outer hair cell motor by membrane cholesterol. *J. Biol. Chem.* 282: 36659–36670.

Rajagopalan, L., L.E. Organ-Darling, H. Liu, A.L. Davidson, R.M. Raphael, W.E. Brownell, and F.A. Pereira. 2010. Glycosylation regulates prestin cellular activity. *J. Assoc. Res. Otolaryngol.* 11:39–51.

Ramamoorthy, S., T.M. Wilson, T. Wu, and A.L. Nuttall. 2013. Non-uniform distribution of outer hair cell transmembrane potential induced by extracellular electric field. *Biophys. J.* 105:2666–2675.

Rodríguez, B.M., D. Sigg, and F. Bezanilla. 1998. Voltage gating of Shaker K+ channels. The effect of temperature on ionic and gating currents. *J. Gen. Physiol.* 112:223–242.

Roux, B.. 2008. The membrane potential and its representation by a constant electric field in computer simulations. *Biophys. J.* 95:4205–4216.

Roy, A., A. Kucukural, and Y. Zhang. 2010. I-TASSER: a unified platform for automated protein structure and function prediction. *Nat. Protoc.* 5:725–738.

Russell, I.J., and M. Kössl. 1992. Voltage responses to tones of outer hair cells in the basal turn of the guinea-pig cochlea: significance for electromotility and desensitization. *Proc. Biol. Sci.* 247:97–105.

Rybalchenko, V., and J. Santos-Sacchi. 2008. Anion control of voltage sensing by the motor protein prestin in outer hair cells. *Biophys. J.* 95:4439–4447.

Santos-Sacchi, J.. 1991. Reversible inhibition of voltage-dependent outer hair cell motility and capacitance. *J. Neurosci.* 11:3096–3110.

Santos-Sacchi, J.. 2002. Functional motor microdomains of the outer hair cell lateral membrane. *Pflugers Arch.* 445:331–336.

Santos-Sacchi, J., and E. Navarrete. 2002. Voltage-dependent changes in specific membrane capacitance caused by prestin, the outer hair cell lateral membrane motor. *Pflugers Arch.* 444:99–106.

Santos-Sacchi, J., and W. Tan. 2018. The Frequency Response of Outer Hair Cell Voltage-Dependent Motility Is Limited by Kinetics of Prestin. *J. Neurosci.* 38:5495–5506.

Santos-Sacchi, J., S. Kakehata, T. Kikuchi, Y. Katori, and T. Takasaka. 1998. Density of motility-related charge in the outer hair cell of the guinea pig is inversely related to best frequency. *Neurosci. Lett.* 256:155–158.

Schänzler, M., and C. Fahlke. 2012. Anion transport by the cochlear motor protein prestin. *J. Physiol.* 590:259–272.

Sfondouris, J., L. Rajagopalan, F.A. Pereira, and W.E. Brownell. 2008. Membrane composition modulates prestin-associated charge movement. *J. Biol. Chem.* 283:22473–22481.

Sigg, D., F. Bezanilla, and E. Stefani. 2003. Fast gating in the Shaker K+ channel and the energy landscape of activation. *Proc. Natl. Acad. Sci. USA.* 100:7611–7615.

Song, L., and J. Santos-Sacchi. 2013. Disparities in voltage-sensor charge and electromotility imply slow chloride-driven state transitions in the solute carrier SLC26a5. *Proc. Natl. Acad. Sci. USA.* 110:3883–3888.

Song, L., and J. Santos-Sacchi. 2015. An electrical inspection of the subsurface cisternae of the outer hair cell. *Biophys. J.* 108:568–577.

Stockard, C.R., and G.N. Papanicolaou. 1919. The Vaginal Closure Membrane, Copulation, and the Vaginal Plug in the Guinea-Pig, with Further Considerations of the œstrous Rhythm. *Biol. Bull.* 37:222–245.

Tan, X., J.L. Pecka, J. Tang, S. Lovas, K.W. Beisel, and D.Z. He. 2012. A motif of eleven amino acids is a structural adaptation that facilitates motor capability of eutherian prestin. *J. Cell Sci.* 125:1039–1047.

Tolomeo, J.A., C.R. Steele, and M.C. Holley. 1996. Mechanical properties of the lateral cortex of mammalian auditory outer hair cells. *Biophys. J.* 71: 421–429.

Triffo, W.J., H. Palsdottir, J. Song, D.G. Morgan, K.L. McDonald, M. Auer, and R.M. Raphael. 2019. 3D Ultrastructure of the Cochlear Outer Hair Cell Lateral Wall Revealed By Electron Tomography. *Front. Cell. Neurosci.* 13: 560.

Vavakou, A., N.P. Cooper, and M. van der Heijden. 2019. The frequency limit of outer hair cell motility measured in vivo. *eLife.* 8. e47667.

von Heijne, G., and Y. Gavel. 1988. Topogenic signals in integral membrane proteins. *Eur. J. Biochem.* 174:671–678.

Wang, X., S. Yang, S. Jia, and D.Z. He. 2010. Prestin forms oligomer with four mechanically independent subunits. *Brain Res.* 1333:28–35.

Wilson, J.P., and J.R. Johnstone. 1975. Basilar membrane and middle-ear vibration in guinea pig measured by capacitive probe. *J. Acoust. Soc. Am.* 57:705–723.

Yamashita, T., J. Fang, J. Gao, Y. Yu, M.M. Lagarde, and J. Zuo. 2012. Normal hearing sensitivity at low-to-middle frequencies with 34% prestin-charge density. *PLoS One.* 7. e45453.

Yang, J., R. Yan, A. Roy, D. Xu, J. Poisson, and Y. Zhang. 2015. The I-TASSER Suite: protein structure and function prediction. *Nat. Methods.* 12:7–8.

Yeung, S.Y., and I.A. Greenwood. 2005. Electrophysiological and functional effects of the KCNQ channel blocker XE991 on murine portal vein smooth muscle cells. *Br. J. Pharmacol.* 146:585–595.

Zagotta, W.N., T. Hoshi, and R.W. Aldrich. 1994. Shaker potassium channel gating. III: Evaluation of kinetic models for activation. *J. Gen. Physiol.* 103:321–362.

Zhang, Y.. 2008. I-TASSER server for protein 3D structure prediction. *BMC Bioinformatics.* 9:40.

Zheng, J., G.G. Du, C.T. Anderson, J.P. Keller, A. Orem, P. Dallos, and M. Cheatham. 2006. Analysis of the oligomeric structure of the motor protein prestin. *J. Biol. Chem.* 281:19916–19924.

Zheng, J., W. Shen, D.Z. He, K.B. Long, L.D. Madison, and P. Dallos. 2000. Prestin is the motor protein of cochlear outer hair cells. *Nature.* 405: 149–155.

Zhu, Y., J. Chen, C. Liang, L. Zong, J. Chen, R.O. Jones, and H.B. Zhao. 2015. Connexin26 (GJB2) deficiency reduces active cochlear amplification leading to late-onset hearing loss. *Neuroscience.* 284:719–729.

Zhu, Y., C. Liang, J. Chen, L. Zong, G.D. Chen, and H.B. Zhao. 2013. Active cochlear amplification is dependent on supporting cell gap junctions. *Nat. Commun.* 4:1786.

Downloaded from http://rupress.org/jgp/article-pdf/152/7/e201912447/1801126/jgp_201912447.pdf by guest on 09 February 2026

Supplemental material

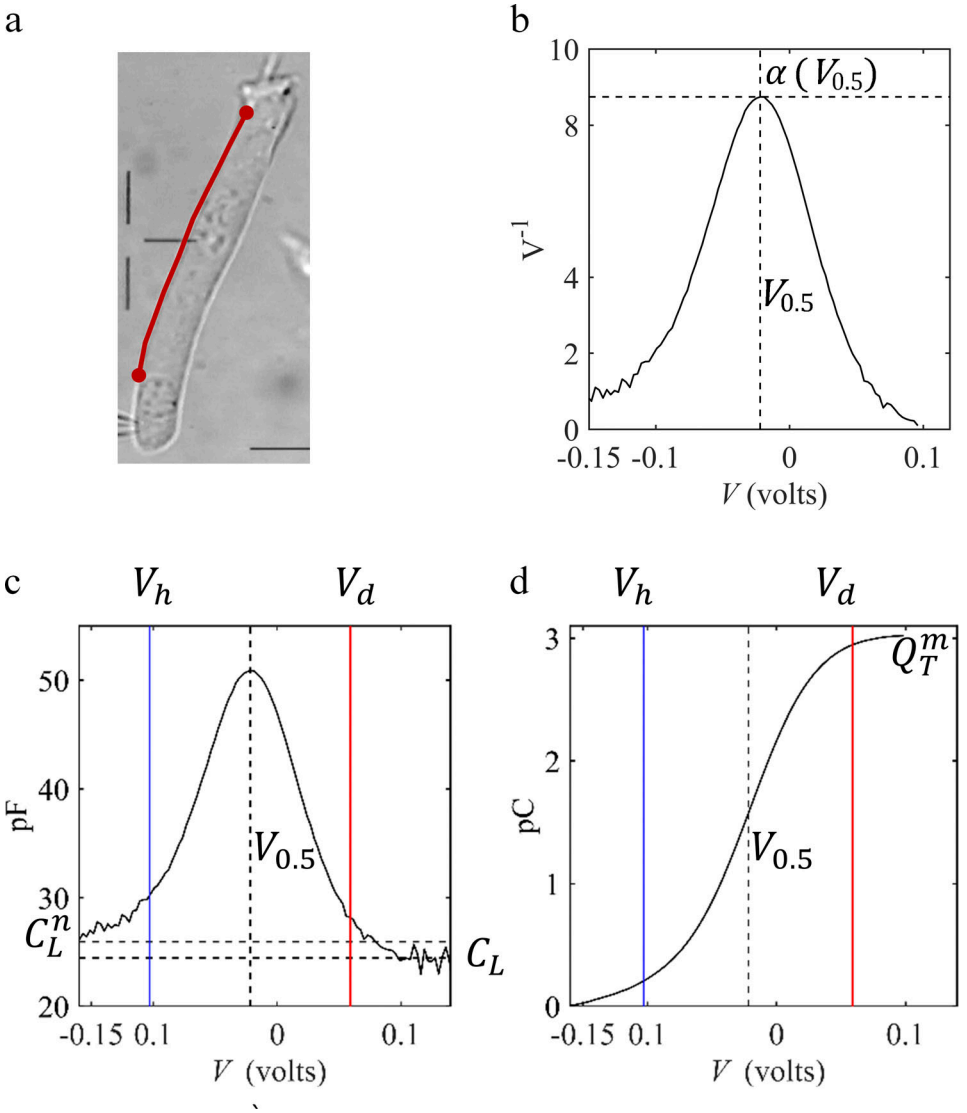

Figure S1. **Example of the electrophysiological data obtained when performing a whole-cell voltage clamp assay on OHC. (a)** Image of OHC showing region where voltage sensors reside (red) on the lateral membrane; scale bar ≡ 10 µm. **(b)** Voltage sensitivity with the maximum value indicated. **(c)** Membrane capacitance determined from admittance measurements. Linear capacitance at positive, C_L, and negative, C_L^n, potentials and $V_{0.5}$ are shown. Red and blue lines indicate calculated pseudo-minima determined with Eq. 3 from measured parameters. **(d)** Maximum charge measured, Q_T^m. Cell (original number 99) was obtained from a juvenile normal (pigmented) female guinea pig, and the experiment was conducted in the presence of 60 µM XEE91. Voltages were corrected for the voltage drop across the pipette where the measured parameters are C_L, 24.45 pF; C_L^n, 25.94 pF; C_{LW}, 18.56 pF; $V_{0.5}$, −0.022 V; Q_T^m, 3.02 pC; and α_B, 34.98 V^{-1}.

Downloaded from http://rupress.org/jgp/article-pdf/152/7/e201912447/1801126/jgp_201912447.pdf by guest on 09 February 2026

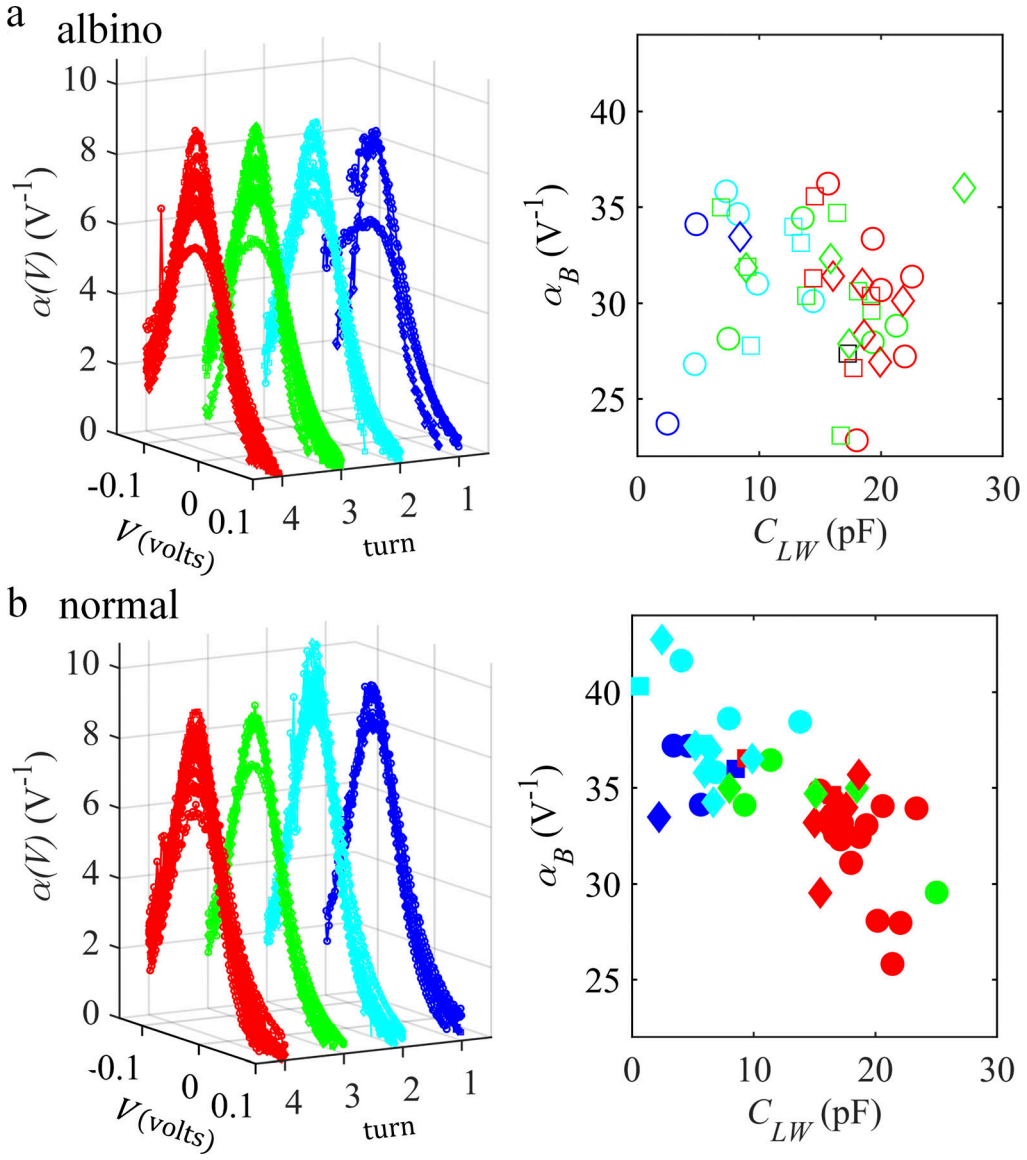

Figure S2. **Voltage sensitivity depends on the positional polarity of the OHC within the cochlea for one guinea pig colony.** Voltage sensitivity for OHCs extracted from albino guinea pigs (a) and for OHCs isolated from normal (pigmented) guinea pigs (b). $V_{0.5}$ was placed at the same voltage for visualization of the data. The right panel shows voltage sensitivity as defined in Eq. 5 and calculated from the data and Eq. 8d as a function of lateral membrane capacitance. The symbols are defined in Fig. 1.

Downloaded from http://rupress.org/jgp/article-pdf/152/7/e201912447/1801126/jgp_201912447.pdf by guest on 09 February 2026

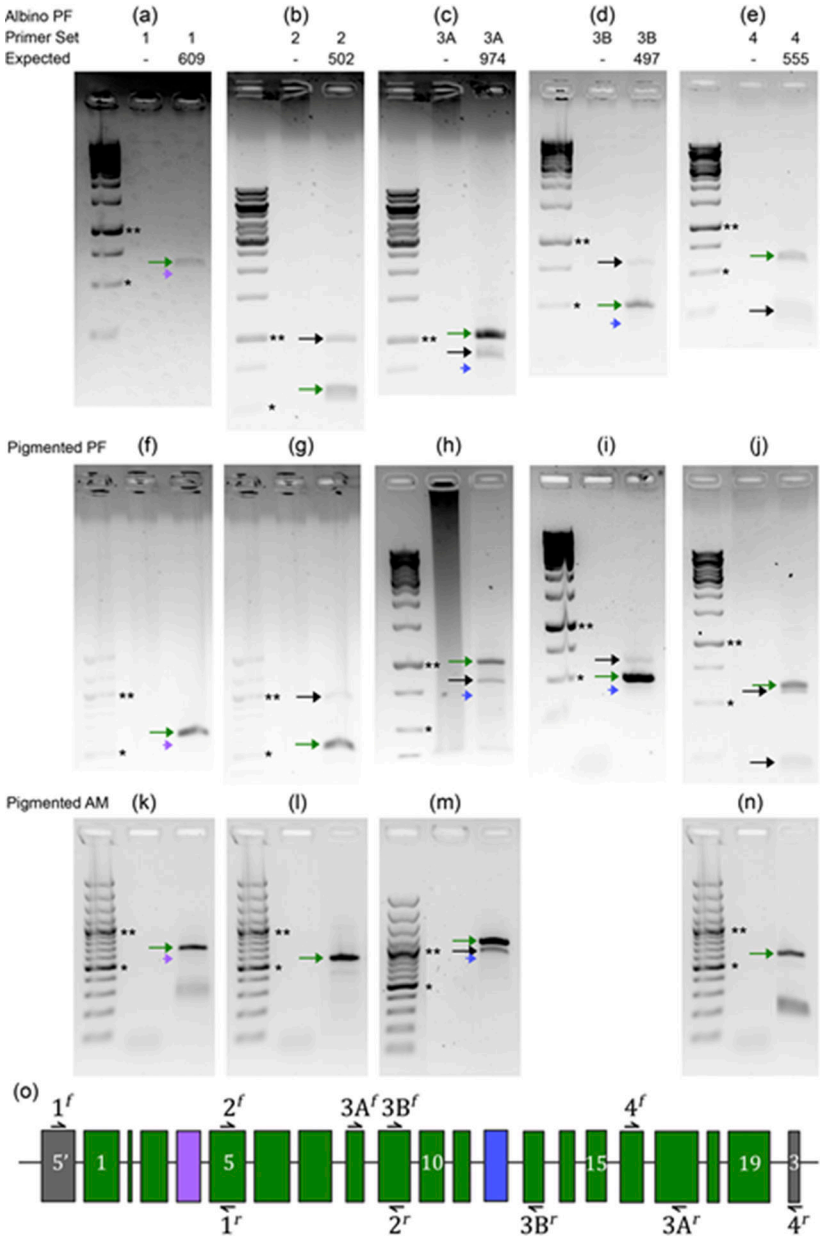

Figure S3. **Only isoform *X1* of guinea pig prestin was found after sequencing. (a–n)** PCR products separated by electrophoresis. The panels represent samples extracted from the cochlea of prepubertal female (PF) albino (a–e), prepubertal female pigmented (f–j), and pigmented adult male (AM; k–n) guinea pigs. In each subpanel, lane 1: ladder (*, 500 bp; **, 1,000 bp), lane 2: negative control (no template DNA), and lane 3: PCR products. Green arrows mark bands confirmed to be PCR products of prestin isoform *X1*. Purple and blue arrowheads mark the expected but absent bp position for isoforms *X3* (primer set 1) and *X2* (primer sets 3A and 3B). Bands marked by black arrows correspond to products of unrelated proteins that were confirmed by sequencing. **(o)** Schematic representation of targets for primer sets used. Green blocks represent exons of isoform *X1*. Purple and blue blocks are absent in isoforms *X3* and *X2*, respectively.

Downloaded from http://rupress.org/jgp/article-pdf/152/7/e201912447/1801126/jgp_201912447.pdf by guest on 09 February 2026

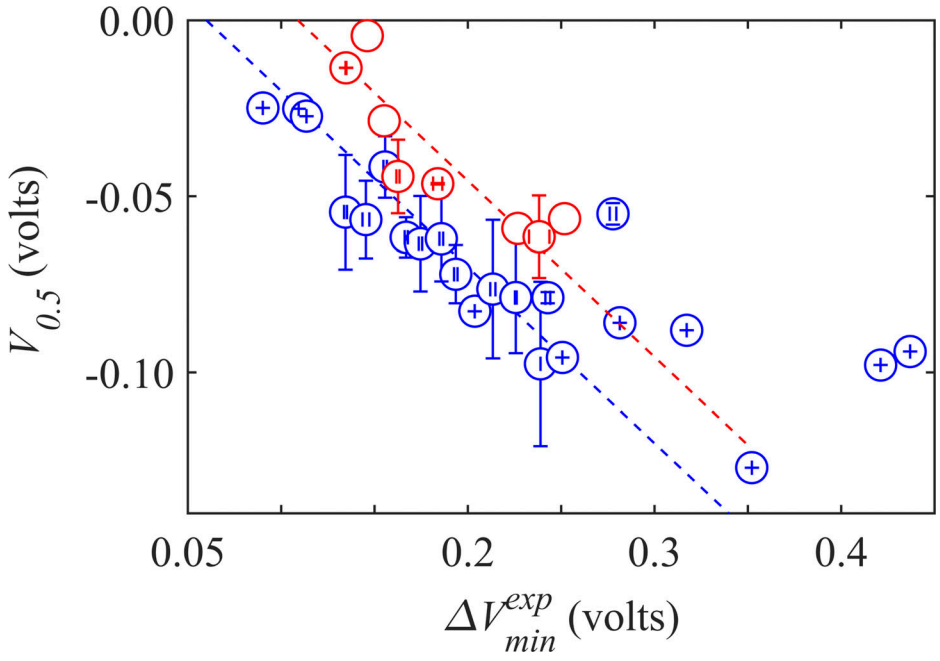

Figure S4. **$V_{0.5}$ as a function of ΔV_{min}^{exp} for OHC data from guinea pigs where data were grouped in smaller increments.** The symbols represent data with (red circles) and without (blue) XE991 in the bath. Data were averaged based on the value of ΔV_{min}^{exp} with a bin width of 0.01 V. The bars are SEM. The dashed blue line was fit to Eq. 3a, where ΔV_{min}^{exp} < 0.4 V was included in the fit. V_d is 0.030 V; adjusted R^2 = 0.389. The dashed red line was fit to Eq. 3a with V_d of 0.054 V; adjusted R^2 = 0.737.

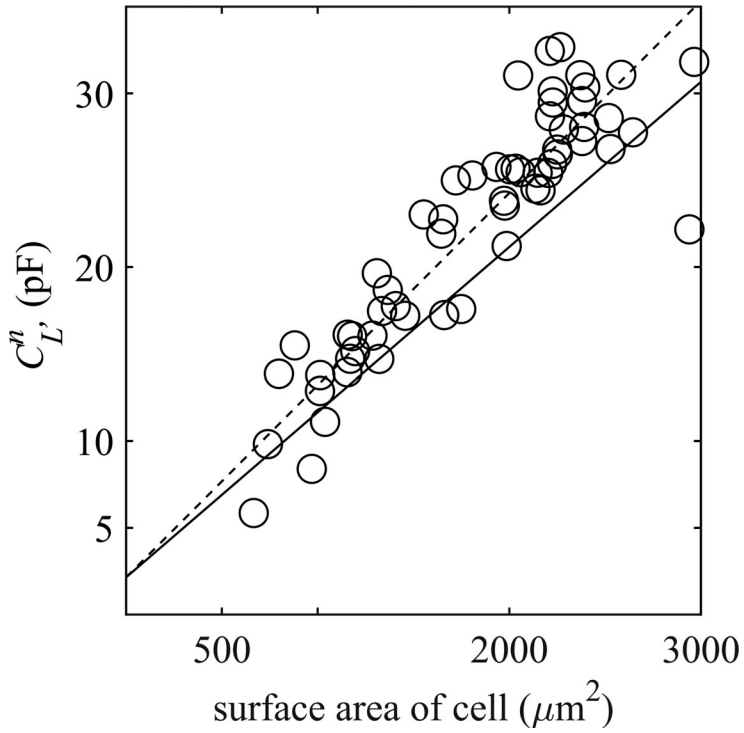

Figure S5. **Voltage-independent membrane capacitance determined at negative voltages (open circles; 59 cells) as a function of the surface area of the cell.** The solid line is fitted to data where capacitance was determined at positive voltages with slope 0.0095 pF/μm^2 and intercept 2.14 pF; adjusted R^2 = 0.79 (83 cells). The dashed line is fit-constrained to the same intercept with slope 0.011062 pF/μm^2; adjusted R^2 = 0.807.

Downloaded from http://rupress.org/jgp/article-pdf/152/7/e201912447/1801126/jgp_201912447.pdf by guest on 09 February 2026

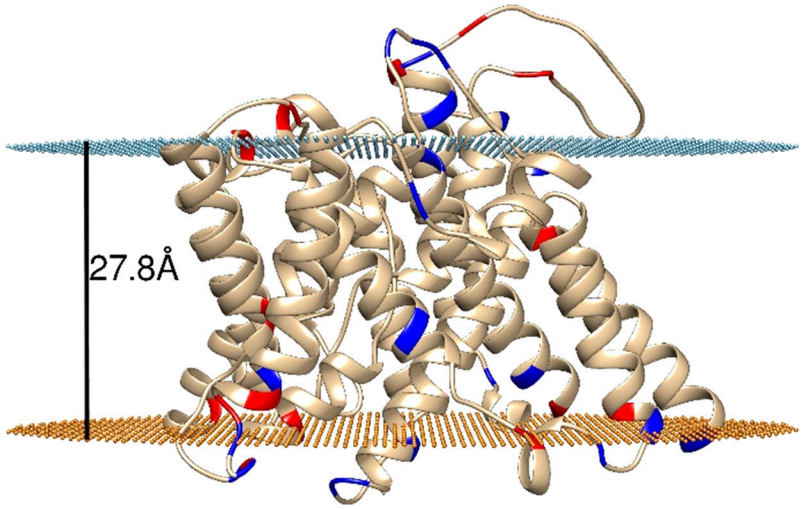

Figure S6. **Model of the transmembrane region of guinea pig prestin shown within a bilayer predicted with the OPM server.** The acidic (red) and basic (blue) titratable residues, as well as the extracellular (cyan) and cytoplasmic (orange) interfaces, are shown.

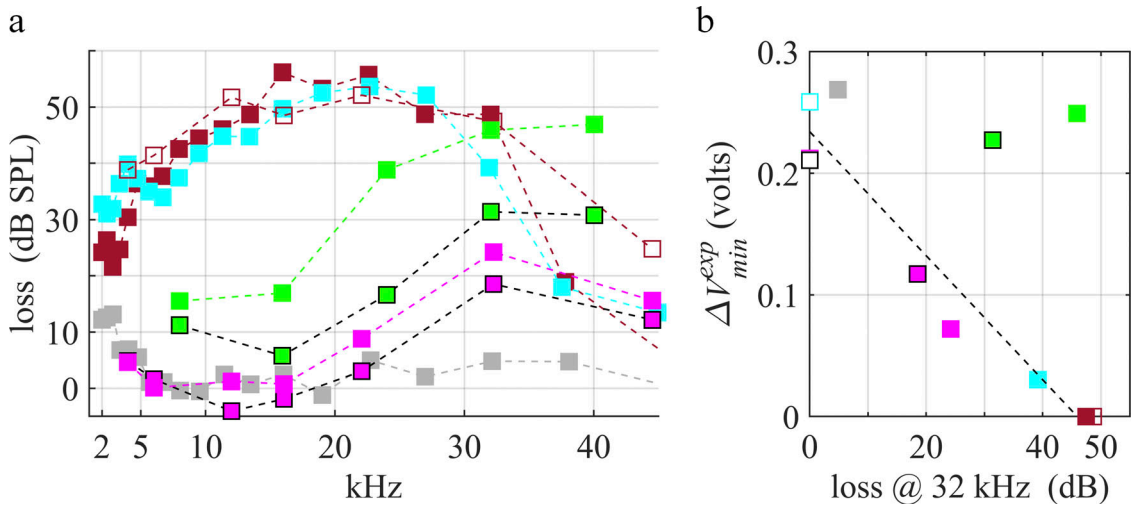

Figure S7. **Hearing loss measured in vivo is correlated to charge density determined from ex vivo preparations of OHCs. (a)** Net hearing loss in mice relative to wild type controls measured with either compound action potential or auditory brainstem response. Solid brown (Dallos et al., 2008) and open brown, prestin KO (Yamashita et al., 2012); cyan, 499 KI (Dallos et al., 2008); solid gray, C1 KI (Gao et al., 2007); magenta with black edges, neo/neo mouse (Yamashita et al., 2012); magenta, neo/prestin KO (Yamashita et al., 2012); green with black edges, connexin 26 hzt (Zhu et al., 2013); and solid green, connexin 26 KO (Zhu et al., 2013). **(b)** The loss at 32 kHz relative to measured experimental charge density. The dashed line represents the best linear fit with a slope of −0.0051 V/dB and intercept 0.2343 V. The open squares are wild type control. See Fig. 3 a for label identification.

Table S1 shows the mean time of recording of OHCs relative to the lifetime temporal boundary of the animal. Table S2 lists primers used to sequence the prestin gene of *C. porcellus*. Table S3 lists the average charge density measurements by region with cells extracted from pigmented phenotype with and without XE991 in bath and measurements with cells extracted from albinos. Table S4 shows the predicted charge of prestin 3D coordinate models created with I-TASSER.

Downloaded from http://rupress.org/jgp/article-pdf/152/7/e201912447/1801126/jgp_201912447.pdf by guest on 09 February 2026